LITHOS

An International Journal of Petrology, Geochemistry and Mineralogy

www.elsevier.com/locate/lithos

(This is a sample cover image for this issue. The actual cover is not yet available at this time.)

ELSEVIER

U–Pb geochronological constraints on the timing of episodic regional metamorphism and rapid high-T exhumation of the Grand Forks complex, British Columbia

J.F. Cubley [a,*], D.R.M. Pattison [a,1], D.K. Tinkham [b,2], C.M. Fanning [c,3]

[a] *Department of Geoscience, University of Calgary, 2500 University Drive NW, Calgary, Alberta, T2N 1N4, Canada*
[b] *Department of Earth Sciences, Laurentian University, 935 Ramsey Lake Road, Sudbury, Ontario, P3E 2C6, Canada*
[c] *Research School of Earth Sciences, Australian National University, Building 61, Mills Road, Acton 0200, Canberra, Australia*

ARTICLE INFO

ABSTRACT

The Grand Forks complex (GFC) is a fault-bounded metamorphic core complex in the southern Omineca Belt of British Columbia, Canada. It experienced prograde metamorphism ranging from upper-amphibolite to granulite facies conditions during the Mesozoic to early Tertiary compressional stage of the Cordilleran orogeny. Peak metamorphism was followed by multi-stage exhumation in the Early Eocene. This study provides U–Pb monazite and zircon constraints on the timing of metamorphic episodes in the GFC and subsequent high-T, amphibolite facies decompression in the Early Eocene. Monazite LA-ICP-MS ages from metapelitic gneisses record episodic metamorphism from the Late Jurassic to Paleocene, with peak metamorphism occurring between ~59 and 50 Ma. Peak metamorphism was followed by rapid, near-isothermal decompression of the GFC between ~52 and 50 Ma, and leucosome crystallization at ~50 Ma. Thermodynamic modeling of metapelites in the system MnNCKFMASHPYCe predicts that monazite was not stable at peak metamorphic conditions, consistent with the dominant population of ~59 Ma ages representing growth along the prograde path, most likely at subsolidus conditions. Growth of widespread high-Y monazite rims (~50 Ma) is predicted along suprasolidus decompression and cooling paths. Zircon SHRIMP ages from igneous bodies in the GFC and hanging wall of the bounding Kettle River fault (KRF) suggest ductile deformation related to high-T decompression of the GFC was ongoing at 51 Ma but had ceased by 50 Ma, truncated by post-kinematic granitoids. This high-T deformation predates subsequent greenschist facies extension on the overlying KRF. A pre-KRF, hanging wall ductile shear zone is constrained to ~59–51 Ma. It deforms 59 Ma Ladybird suite leucogranites and may be related to high-T exhumation of the core complex. Rapid, >100 °C/Ma cooling rates are required to accommodate high-T (amphibolite facies) exhumation of the GFC at 52–50 Ma followed by low-T (greenschist facies) exhumation at ~49 Ma.

1. Introduction

The Grand Forks complex (GFC) is a fault-bounded metamorphic core complex in southeastern British Columbia. It exposes high-grade, upper-amphibolite to granulite facies lithologies in a broad structural dome (Armstrong et al., 1991; Höy and Jackaman, 2005a; Preto, 1970). The GFC is known as the Kettle dome or Kettle complex south of the United States–Canada border (Cheney, 1980; Kruckenberg et al., 2008; Orr and Cheney, 1987). The Grand Forks complex is bounded on its east side by the Kettle River fault (KRF) system, an east-dipping fault zone with ductile and brittle features, and on its west side by the predominantly brittle, west-dipping Granby fault (GF). High-grade rocks of the GFC are juxtaposed across these faults against low-grade, greenschist to lower-amphibolite facies volcanics, volcaniclastics, and metasediments of the pericratonic Quesnel terrane (Acton et al., 2002; Cubley and Pattison, in press; Fyles, 1990; Laberge and Pattison, 2007; Unterschutz et al., 2002).

The GFC is located in the southern Omineca belt, the crystalline hinterland to the foreland fold and thrust belt of the Canadian Cordillera (Fig. 1). In southeastern British Columbia, Washington, and Idaho, the Omineca Belt contains a number of metamorphic core complexes (Fig. 1) known collectively as the Shuswap complex or Shuswap domain (e.g. Monger et al., 1982). As with other metamorphic core complexes within the Shuswap domain, the Grand Forks complex experienced compressional deformation and metamorphism during late Mesozoic to early Tertiary Cordilleran orogenesis, followed by Eocene extension beginning at ca. 55–52 Ma (Brown and Journeay, 1987; Parrish et al., 1985, 1988; Teyssier et al., 2005; Vanderhaeghe and Teyssier, 2001; Vanderhaeghe et al., 1999). The current study focuses on the southernmost portion of the Canadian extent of the GFC,

* Corresponding author at: School of Mining and Technology, Yukon College, 500 College Drive, Whitehorse, Yukon Territory, Y1A 5K4, Canada. Tel.: +1 867 456 8605.
 E-mail addresses: jcubley@yukoncollege.yk.ca (J.F. Cubley), pattison@ucalgary.ca (D.R.M. Pattison), dtinkham@laurentian.ca (D.K. Tinkham), Mark.Fanning@anu.edu.au (C.M. Fanning).
 [1] Tel.: +1 403 220 3263.
 [2] Tel.: +1 705 675 1151x2270.
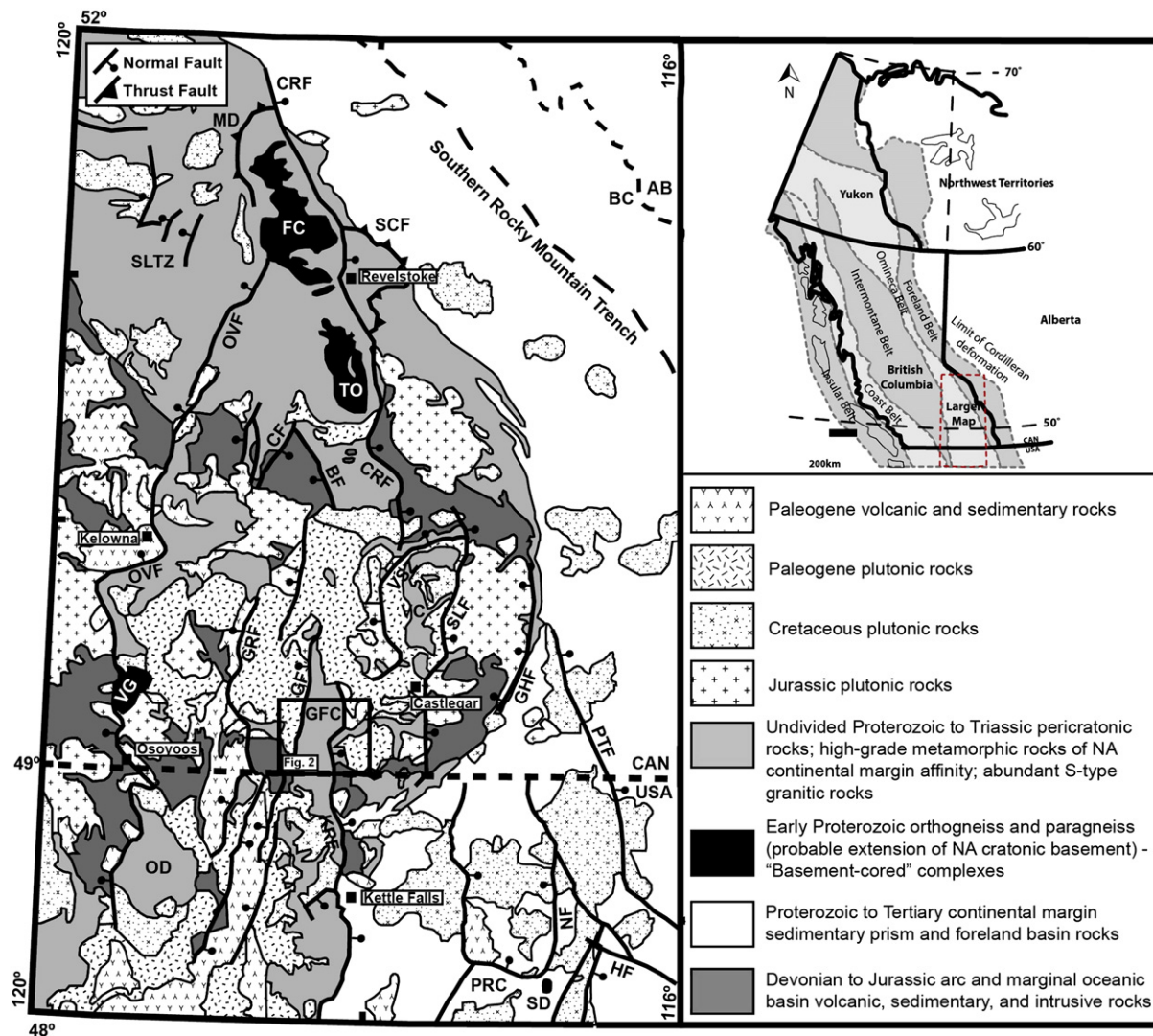 [3] Tel.: +61 02 6125 5507.

Fig. 1. Regional map of the southern Canadian Cordillera, adapted from Glombick et al. (2006), after Wheeler and McFeely (1991). Western Canada map after Johnson and Brown (1996). The study area in the northern Grand Forks/Kettle complex is shown by the black rectangle entitled Fig. 2. Abbreviations: BF = Beaven fault, CF = Cherry–Cherryville fault, CRF = Columbia River fault, ERF = Eagle River fault, FC = Frenchman Cap dome, GF = Granby fault, GFC = Grand Forks complex, GHF = Gallagher fault, GRF = Greenwood fault, HF = Hope fault, KRF = Kettle River fault, MD = Monashee décollement, NA = North America, NF = Newport fault, OD = Okanagan dome, OVF = Okanagan Valley fault, PRC = Priest River complex, PTF = Purcell Trench fault, SCF = Standfast Creek fault, SD = Spokane dome, SLF = Slocan Lake fault, SLTZ = Shuswap Lake transfer zone, TO = Thor-Odin dome, VC = Valhalla complex, VG = Vaseaux gneiss, VSZ = Valkyr shear zone.

corresponding roughly to the NTS 082E/01 1:50,000 map sheet and bounded by the villages of Christina Lake and Grand Forks (Fig. 2).

This paper presents new U–Pb zircon and monazite ages from the Grand Forks complex, combined with thermodynamic modeling of monazite paragenesis in pelitic gneisses. These data provide new insights into the timing and nature of metamorphism and high-temperature exhumation in the GFC, and more generally on the petrogenetic behavior of monazite at suprasolidus conditions. This information helps address a gap in understanding of regional exhumation of the southern Shuswap complex, and helps link recent advances in the nearby Valhalla complex (e.g. Gordon et al., 2008; Hallett and Spear, 2011; Simony and Carr, 2011) and Okanogan dome (Kruckenberg and Whitney, 2011; Kruckenberg et al., 2008).

2. Regional geology

2.1. Grand Forks complex

In southern British Columbia, the Grand Forks complex (GFC) forms a broad, N–S trending structural dome bounded on the east

and west by Eocene normal fault systems (Fig. 2). A schematic cross section showing the approximate positions of dated monazite and zircon samples from the GFC within this domal structure is shown in Fig. 3. The dome plunges shallowly to south, with the deepest stratigraphic levels exposed in British Columbia and stratigraphically higher rocks common south of the border in Washington (Cheney, 1980; Orr and Cheney, 1987; Preto, 1970). Paleoproterozoic to lower Paleozoic pelites, amphibolites, calc-silicates, quartzites, and marbles of the Grand Forks Group are exposed within the core complex. These have been intruded by granitic to tonalitic Neoproterozoic to Paleozoic intrusives (Armstrong et al., 1991; Höy and Jackaman, 2005a; Preto, 1970; Ross and Parrish, 1991).

Metamorphism in the Grand Forks complex is predominantly upper-amphibolite to granulite facies, manifested by Sil + Kfs ± Grt ± Crd-bearing assemblages (mineral abbreviations after Kretz, 1983) in migmatitic pelitic gneisses (Fig. 4a,b) (Cubley and Pattison, in press; Laberge and Pattison, 2007). On the eastern margin of the core complex, Cpx + Opx-bearing granulite facies assemblages occur locally in amphibolites (Cubley and Pattison, 2009, in press). The pressure–temperature conditions for the peak pelitic metamorphic
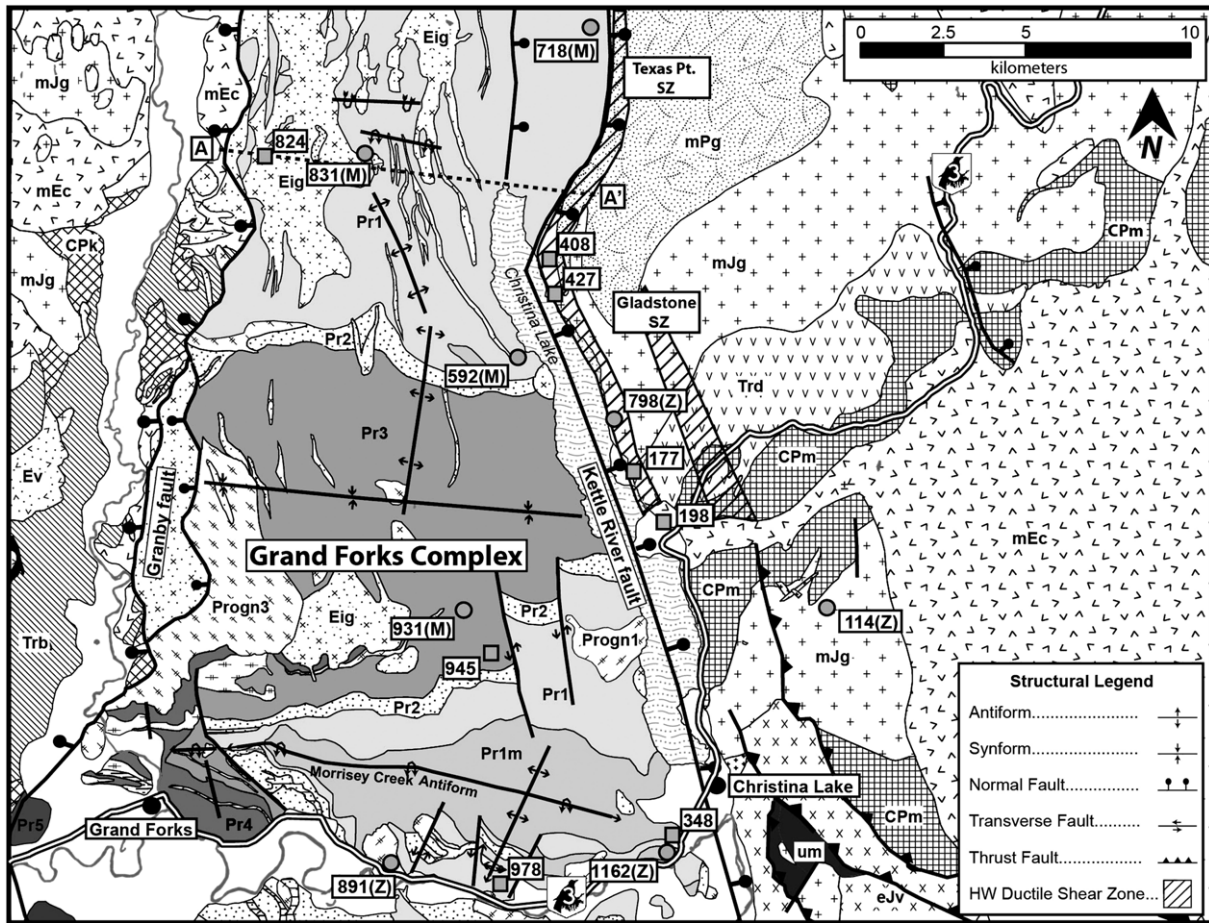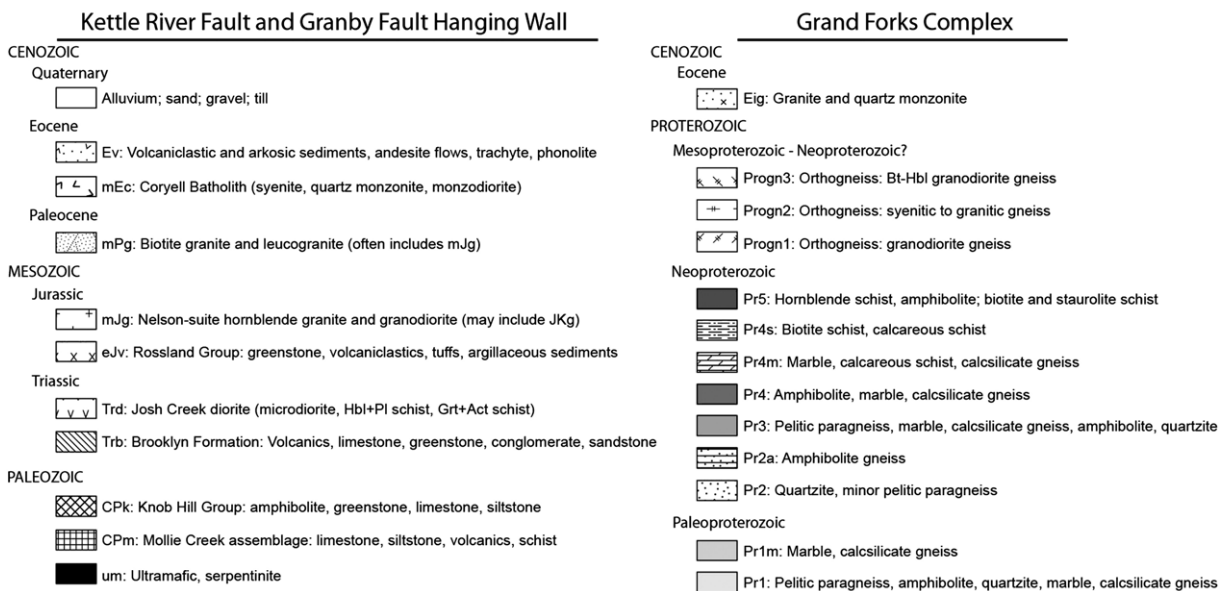
Fig. 2. Simplified geology map of the Grand Forks 1:50,000 map sheet (NTS 82E/01), adapted from the compilation of Höy and Jackaman (2005b). U–Pb zircon (Z) and monazite (M) geochronology sample locations are shown (circles), as well as structural localities referred to in the text (squares). The cross section line in Fig. 3 is shown (A–A′). SZ = shear zone.

assemblage have been constrained to between 750–800 °C and 5.5–6.0 kbar (Cubley and Pattison, 2009, in press; Laberge and Pattison, 2007). Metamorphic grade decreases to the southwest towards higher structural and stratigraphic levels, with middle-amphibolite St + Bt ± Sil and Grt + Bt schists preserved just west of the town of Grand Forks (unit Pr5) (Cubley and Pattison, in press; Preto, 1970). In GFC migmatitic paragneisses, Crd + Ilm + Spl ± Rt reaction textures around sillimanite and Crd + Qtz coronas around garnet suggest high-temperature (~725–750 °C), near-isothermal decompression (Cubley and Pattison, in press; Laberge and Pattison, 2007). In metabasites, this episode of decompression resulted in Cpx + Opx + Pl + Mt symplectites after garnet (Cubley and Pattison, in

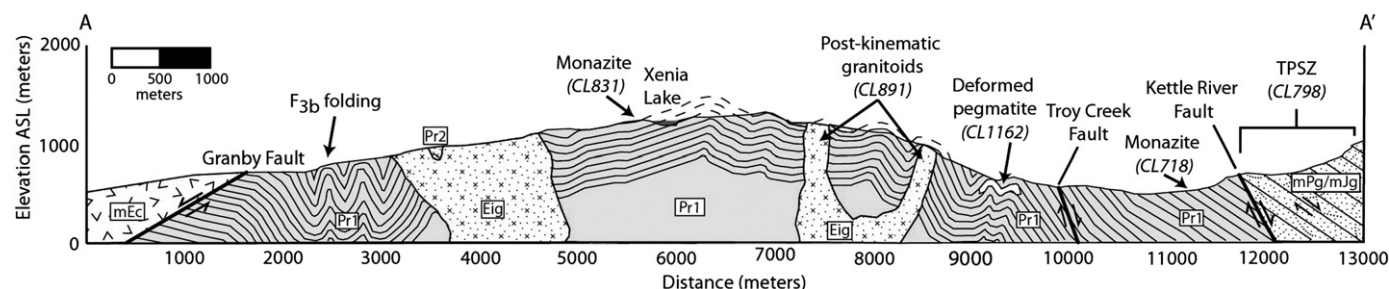**Fig. 3.** East–west cross section across the Grand Forks complex, corresponding to line A–A′ in Fig. 2, based on compilation mapping of Höy and Jackaman (2005b) and new mapping from this study. The relative structural positions of dated zircon samples (CL891, CL1162 and CL798) and monazite sample CL718 are shown, though those samples lie outside the plane of the cross section.

press). Pressure–temperature estimates for the high-temperature, low-pressure assemblages are 725–800 °C and 3.2–4.2 kbar (Cubley and Pattison, 2009, in press; Laberge and Pattison, 2007).

Localized shear zones arch across the dome in British Columbia, and have been attributed to high-T deformation (Cubley and Pattison, in press; Preto, 1970; Simony and Carr, 2011). These high-strain fabrics post-date the development of the predominant gneissic fabric (S_2) and typically show top-to-the-east shear sense indicators, though isolated zones of antithetic shear have been observed. Mineral elongation lineations (Sil, Hbl, Qtz) within these fabrics trend predominantly E–W.

The core complex has experienced multiple folding episodes observable from outcrop to map scales (Figs. 2, 4c), with the major folding episodes predating greenschist facies extension on the KRF and GF (Cubley and Pattison, in press; Preto, 1970). The dominant folding episode, F_{3a}, is characterized by outcrop- to map-scale upright to inclined folds (e.g. the Morrisey Creek Antiform, Fig. 2) with E–W fold axes (Cubley and Pattison, in press). Folding postdates the development of ductile shear zones in the Grand Forks complex, but is truncated by the intrusion of post-kinematic granitic to monzonitic intrusives (Fig. 4c) (Cubley and Pattison, in press; Preto, 1970).

The eastern margin of the core complex is defined by the east-dipping Kettle River fault (KRF), which extends north and south of the study area for a total strike length of ~95 km (Figs. 1, 2). In NE Washington (Mulch et al., 2007; Orr and Cheney, 1987; Rhodes and Cheney, 1981), the fault is a brittle–ductile greenschist facies (~415 °C) extensional system (Mulch et al., 2007). In the stratigraphically lower rocks exposed in British Columbia, footwall mylonitic fabrics attributed to the KRF in Washington are not developed, and brittle deformation fabrics associated with the fault cut high-temperature footwall gneissic fabrics at a high angle (Cubley and Pattison, in press; Rhodes and Cheney, 1981).

The western margin of the core complex is defined by the Granby fault, a shallowly west-dipping listric normal fault that displays predominantly brittle fabrics. Isolated thin footwall mylonites have been documented (Carr and Parkinson, 1989; Fyles, 1990; Laberge and Pattison, 2007; Preto, 1970). South of the border, the Granby fault (GF) forms the eastern margin of the Republic Graben, a syn-extensional rift basin (Suydam and Gaylord, 1997). Brittle movement on both the Kettle River fault and Granby fault postdates the intrusion of 51.1 ± 0.5 Ma alkalic intrusives of the Coryell suite (Acton, 1998; Carr and Parkinson, 1989; Cubley and Pattison, in press).

The large metamorphic contrast across the Kettle River and Granby normal faults suggests significant exhumation of the Grand Forks complex, on the order of ~3–3.5 kbar (Cubley and Pattison, 2009, in press; Laberge and Pattison, 2007). This exhumation was accommodated by sequential high-temperature (amphibolite facies) and low-temperature (greenschist facies) exhumation events (Cubley and Pattison, 2009, in press; Laberge and Pattison, 2007). The timing of low-temperature extension on the KRF has been dated to ~49 Ma in Washington state using $^{40}Ar/^{39}Ar$ geochronology of

muscovite in mylonitic quartzites (Berger and Snee, 1992; Mulch et al., 2007). However, the timing of the high-temperature exhumation episode and its relationship to peak metamorphism and high-T deformational fabrics is poorly constrained.

2.2. Low-grade metamorphic rocks in GF and KRF Hanging Walls

Low-grade metamorphic and intrusive rocks in the hanging walls of the Granby and Kettle River faults have been described by a number of authors, including Acton (1998), Acton et al. (2002), Cubley and Pattison (2009), Fyles (1990), Höy and Jackaman (2005a), and Laberge and Pattison (2007). The current study provides new U–Pb zircon data for igneous intrusives in the KRF hanging wall, building on U–Pb geochronology by Acton et al. (2002). The stratigraphy in the hanging wall of the KRF in British Columbia consists of a sedimentary, volcanic, and volcaniclastic succession deposited mainly during the Carboniferous to Early Jurassic (Acton et al., 2002; Höy and Dunne, 1997; Höy and Jackaman, 2005a). In the Christina Lake area, this sequence is dominated by metasedimentary rocks of the Pennsylvanian–Permian Mollie Creek assemblage and metavolcanic and volcaniclastic rocks of the Early Jurassic Elise Formation of the Rossland Group (Acton, 1998; Acton et al., 2002).

Four intrusive suites have been emplaced into these country rocks: 1) the ~216 Ma Triassic Josh Creek diorite (Acton et al., 2002), 2) granites and granodiorites correlated with the ~173–159 Ma Middle Jurassic Nelson Suite (e.g. Ghosh, 1995; Parrish, 1992b), 3) syenites and monzonites of the Eocene Coryell Batholith (Carr and Parkinson, 1989), and 4) leucocratic granites of unknown age located to the northeast of Christina Lake (Fig. 2). The leucocratic granites resemble post-kinematic granitoids in the GFC and have been correlated with the Jura-Cretaceous composite Okanagan Batholith (Höy and Jackaman, 2005b; Tempelman-Kluit, 1989), or alternatively with the Paleocene–Eocene Ladybird intrusive suite (Acton et al., 2002).

Rocks in the hanging wall of the KRF were folded, faulted, and metamorphosed at upper-greenschist to transitional amphibolite facies in the Middle Jurassic, prior to the intrusion of the Nelson intrusive suite (Acton, 1998; Acton et al., 2002; Cubley and Pattison, in press; Höy, 2006). Jurassic-aged contact metamorphism is observed in a poorly-defined contact aureole surrounding the Nelson intrusive suite east of Christina Lake (Cubley and Pattison, in press). Two east-dipping, normal-sense shear zones occur in the immediate hanging wall to the brittle KRF; the Texas Point shear zone (TPSZ) and Gladstone shear zone (GSZ) (Fig. 2) (Cubley and Pattison, in press). These locally deform the Josh Creek diorite, Mollie Creek assemblage, Nelson-suite intrusives, and unconstrained leucogranites northeast of Christina Lake (Fig. 4d,e). In turn, these ductile deformation fabrics are truncated by undeformed Eocene Coryell intrusives (Fig. 4f). All rocks are deformed by late brittle deformation on the KRF (Fig. 4h) (Cubley and Pattison, in press).

Fig. 4. Field photographs of lithologies from the GFC and bounding fault zones. Site localities are shown in Fig. 2. (a) CL945: Typical Grt-rich Sil + Grt + Kfs GFC paragneiss with stromatic leucosome. (b) CL978: Ductilely deformed granitic leucosome in Grt + Bt orthogneiss, with small-scale folds that have E–W trending F_{3a} fold axes. Partial melting predates fold development. (c) CL348: Mylonitic calc-silicate gneiss folded by F_{3a} fold; fabrics are truncated by Eocene leucogranite. Picture facing 180. (d) CL408: Jurassic Nelson suite Hbl + Bt granodiorite from the Texas Point shear zone (TPSZ) in the hanging wall of the KRF. Shear sense indicators suggest top-to-the-east movement. Leucocratic layers are correlated with the Ladybird intrusive suite. (e) Highly strained Josh Creek microdiorite in the TPSZ, hanging wall of the KRF. (f) CL198: Massive, undeformed Coryell suite monzonite that crosscuts the TPSZ near Texas Point (Fig. 2). (g) CL824: Brittlely deformed GFC footwall granite in the Granby fault zone. (h) CL427: Brittle deformation of massive hanging wall leucogranite in the Kettle River fault zone, northeastern shore of Christina Lake.

3. U–Pb monazite geochronology

A previous study of monazite geochronology in the Grand Forks complex by Laberge and Pattison (2007) identified Late Cretaceous peak metamorphism at 84 ± 3 Ma, followed by minor recrystallization of monazite at 51 ± 2 Ma resulting from the regional emplacement of the Coryell Batholith (Carr and Parkinson, 1989). This age of peak metamorphism differs from peak metamorphic ages determined for other complexes within the composite Shuswap complex that suggest peak metamorphism occurred between ~60 and 55 Ma (e.g. Crowley and Parrish, 1999; Glombick et al., 2006; Gordon et al., 2008; Hinchey et al., 2007; Kruckenberg et al., 2008; Parrish, 1995; Spear and Parrish, 1996). Combining their monazite data with previously published hornblende K–Ar data, Laberge and Pattison (2007) proposed slow-cooling following near-isothermal decompression in the Late Cretaceous. In contrast, other studies of the Shuswap complex (e.g. Gordon et al., 2009; Hinchey et al., 2007; Norlander et al., 2002; Vanderhaeghe et al., 2003), as well as recent modeling by Rey et al. (2009), suggest that rapid cooling followed high-T decompression.

3.1. Methods

Four $Sil + Grt + Bt + Crd + Kfs + Pl + Qtz + Ilm \pm Spl \pm Rt$-bearing metapelitic gneiss samples were chosen for monazite dating, three from the basal paragneiss unit of the Grand Forks Group (unit Pr1; CL592, CL718, CL831) and one sample from the intermediate paragneiss unit (unit Pr3; CL718) (Fig. 2). Monazites in schists from the uppermost pelite unit of the GFC (unit Pr5) were found to be too small ($<10 \, \mu m$ wide) for isotopic analysis. Paragneiss samples were chosen for their 1) high number of monazite grains (≥ 20 grains per standard sized thin section), 2) migmatitic textures with distinct melanosome and leucosome banding, and 3) the presence of microtextures related to high-T decompression, namely $Crd + Ilm + Spl$ coronas around sillimanite and $Crd + Qtz$ coronas around garnet (Fig. 5). Understanding the timing of monazite growth relative to the formation of specific microtextures was critical for delineating relationships between monazite growth, prograde and retrograde metamorphism, and anatexis.

3.1.1. Paragneiss sample descriptions

The mineralogy and microtextures of migmatitic paragneisses from the Grand Forks complex are described in detail by Cubley and Pattison (in press) and Laberge and Pattison (2007). Samples specific to this study are characterized by $Kfs + Qtz$-rich leucosome layers alternating with melanosome dominated by $Sil + Grt + Bt + Crd + Pl + Ilm + Spl$ (Fig. 5a,b). A monomineralic biotite selvage locally separates the leucosome from the melanosome (Fig. 5a). Sillimanite in melanosome layers forms euhedral, prismatic crystals surrounded by a $Crd + Ilm + Spl \pm Rt$ retrograde reaction texture (Fig. 5a,b). In places where this reaction texture is not well-developed, sillimanite forms discrete layers with plagioclase and biotite (Fig. 5c). Anhedral garnet grains are located on the edges of melanosomes or in $Pl + Qtz$-rich psammitic layers. Garnets are typically embayed with retrograde reaction coronas of pinitized cordierite and quartz (Fig. 5f). Samples CL592 and CL931 contain anhedral, matrix cordierite grains unrelated to garnet or sillimanite. This cordierite is observed near melanosome–leucosome boundaries or within diffuse, psammitic melanosome layers. Biotite is concentrated in melanosome layers as strongly oriented grains parallel to the foliation, but is also observed as smaller, randomly oriented grains in leucosome layers. Biotite within monomineralic selvages is noticeably coarser than elsewhere in thin section and is poorly oriented with respect to the foliation, suggesting selvage formation occurred late in the tectonic evolution of the dome. Monazite grains in paragneiss samples are predominantly found in four textural locations: 1) in pinitized cordierite in $Crd + Ilm + Spl + Rt$ reaction textures around sillimanite (Fig. 5b,d); 2) in partially to completely pinitized cordierite around garnet (Fig. 5f); 3) as inclusions or along grain boundaries in $Bt + Kfs + Qtz$ leucosome layers; or 4) as inclusions within biotite selvages, often in close association with zircon and late allanite alteration (Fig. 6a,b)).

3.1.2. Monazite analytical procedures

Paragneiss samples were characterized petrographically, and each full thin section was mapped for Ce and P on the JEOL JXA-8200 electron microprobe at the University of Calgary. Monazite grains were identified using the full thin section chemical maps and energy dispersive spectrometry (EDS). Backscattered electron (BSE) images were then taken of all monazites at a number of magnifications to identify both their textural setting and zoning as a function of mean atomic number. The textural settings of all monazites analyzed in this study are detailed in Cubley (2012). Those monazites that A) showed coherent zoning patterns and B) had chemical zones large enough to accommodate individual laser ablation spots were X-ray mapped at high resolution for Ce, La, Nd, Th, U, Ca and Y. Representative BSE and yttrium X-ray chemical maps are shown in Fig. 7, with the full suite of X-ray maps for those monazites included in Appendix A. All X-ray mapping was conducted with an accelerating voltage of 15 kV and a beam current of 50 nA. The chemical maps have standardized scales (raw counts) allowing direct comparisons between grains. The BSE images in combination with the chemical maps were used to direct subsequent LA-ICP-MS dating.

Monazite dating was conducted at the radiogenic isotope facility of the University of Alberta, Edmonton using in-situ laser ablation–multiple collector–inductively coupled plasma–mass spectrometry (LA-MC-ICP-MS). Instrumentation at the University of Alberta includes a Nu Plasma MC-ICP-MS coupled to a Nd:YAG laser ablation system. The instrument is equipped with a modified collector block including 12 Faraday collectors and three ion counters (Simonetti et al., 2005), and analytical and instrumentation protocol follows Simonetti et al. (2006). A total of 213 ablation analyses were acquired on 69 grains analyzed in the four thin sections. Spot analyses (ablation pits) were 16 μm in diameter. Calibration is relative to a reference "Madagascar monazite" with an age of 512.7 ± 1.8 Ma (Simonetti et al., 2006).

Complete monazite geochronological results are presented in Appendix B, with isotopic ratios uncorrected for common Pb and errors reported at the 2σ level. Tera–Wasserburg U–Pb concordia plots (Fig. 8) (Tera and Wasserburg, 1972), weighted mean $^{206}Pb/^{238}U$ ages, and probability–density diagrams (Fig. 9) were constructed using ISOPLOT v. 3.0 (Ludwig, 2003). Tera–Wasserburg diagrams were constructed using uncorrected U–Pb data. The data fall on or just above the concordia, with the latter likely due to common lead contamination (e.g. Dickin, 2005). The $^{206}Pb/^{238}U$ ages reported in the probability–density diagrams in Figs. 9 and 10 have been corrected for common Pb using the ^{204}Pb method (Williams, 1998 and references therein). Diffusive Pb loss is considered negligible because of sharp interfaces between domains, and previous results showing that monazite is resistant to thermally induced volume diffusion below ~900 °C (e.g. Braun et al., 1998; Cherniak et al., 2004).

3.2. Monazite geochronology results

3.2.1. Monazite populations in Grand Forks complex paragneisses

A summary of the petrographic and chemical features of GFC monazite populations is presented in Table 1, as well as a breakdown of the individual age populations constrained by LA-ICP-MS analysis. Errors reported for monazite age populations are 2σ standard errors of the weighted mean $^{206}Pb/^{238}U$ ages, as calculated via ISOPLOT (Ludwig, 2003). Individual spot analyses were assigned to age populations based on the following criteria: 1) chemical signature relative to surrounding domains in X-Ray chemical maps (Fig. 7; Appendix A); 2) relative intensities in BSE images; 3) textural location, both within a single monazite grain (e.g. core vs. rim domain) and in the rock matrix (e.g. unzoned grain in stromatic
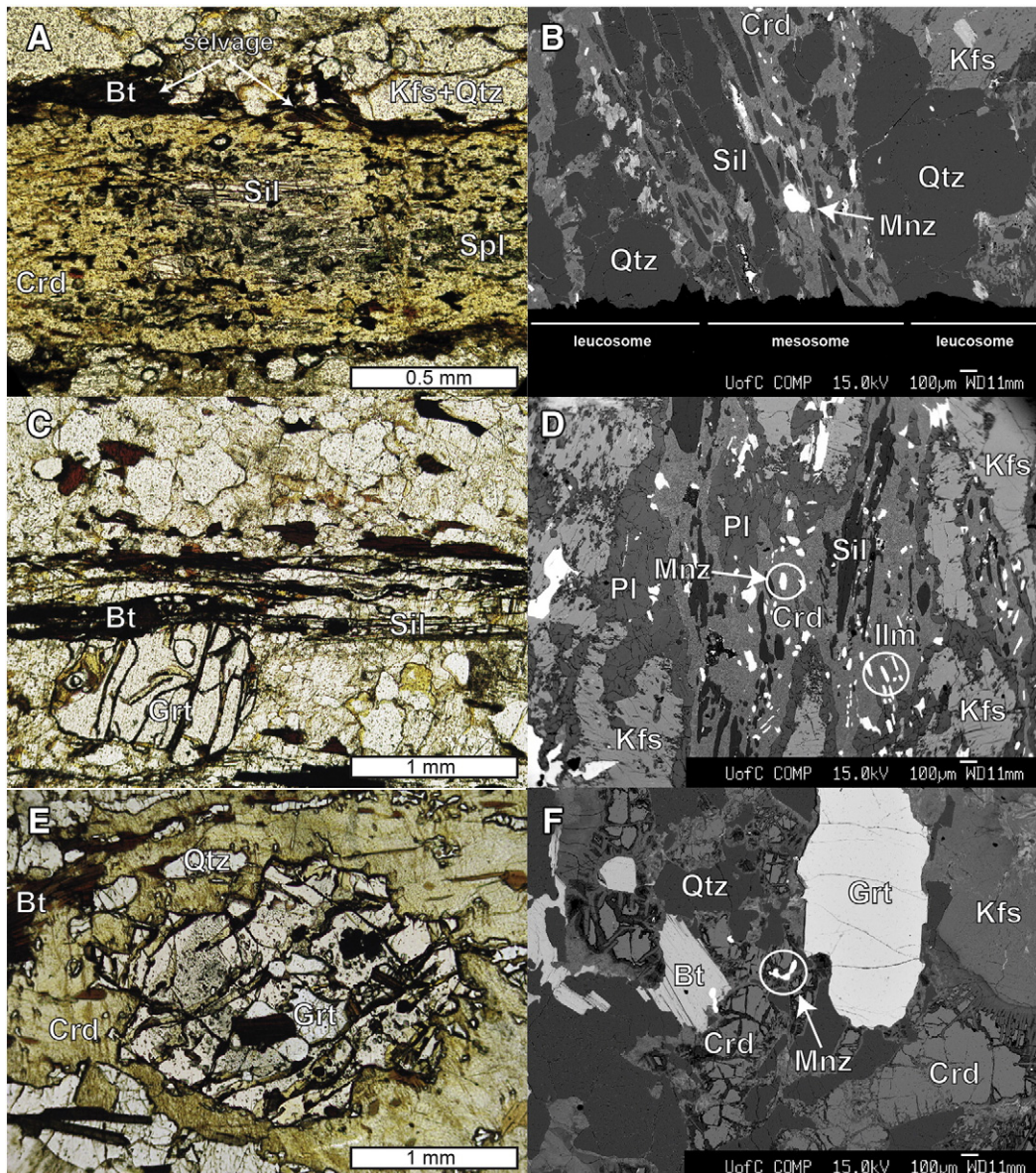
Fig. 5. Photomicrographs and backscattered electron (BSE) images from GFC paragneiss samples. (a) CL592: Photomicrograph of sillimanite-rich paragneiss shows monomineralic biotite selvage separating Kfs + Qtz-rich leucosome from Sil + Crd + Bt + Ilm + Spl-bearing melanosome. (b) CL592: BSE image shows melanosome and leucosome gneissic layering, with large monazite as inclusion within partially pinitized cordierite of Crd + Ilm + Spl reaction corona. (c) CL718: Photomicrograph of paragneiss showing the peak metamorphic assemblage, with unaltered garnet, biotite, and sillimanite in thin melanosome layers. (d) CL831: BSE image of Crd + Ilm + Spl reaction textures around sillimanite, with monazite present within pinitized cordierite. (e) CL831: Photomicrograph of poikiloblastic garnet in that is embayed and surrounded by Crd + Qtz reaction corona. (f) CL931: BSE image showing embayed garnet surrounded by Crd + Qtz reaction texture, with cordierite less pinitized than in (f). Monazite lies within the cordierite.

leucosome vs. resorbed rim in melanosome); and 4) the U–Pb analysis date. Despite the thin growth zones in GFC monazites, the replication of U–Pb dates is taken to be an indication that the ages represent a single growth age, instead of mixed ages, because it is unlikely that numerous spots would contain identical mixtures of multiple age domains. Analysis spots that clearly overlap chemical zones in BSE images (~25% of the 213 total analyses) were not included in the calculation of individual population ages. Whereas these approaches do not eliminate the potential for mixing in the third dimension, they appear to highlight the main growth episodes. Interpretations of the age populations with respect to chemical domains are shown in Fig. 7.

Monazite grains in CL592 range from unzoned to relatively simple with distinct cores and rims (Fig. 7a,b), to complex grains with patchy internal zoning. Most grains are anhedral to subhedral with significant resorption, however a small number of euhedral grains with

concentric zoning were observed, composed predominantly of ~95 Ma and ~60 Ma age domains. Fifty-four "single-domain" analysis spots were recorded on 18 individual grains (Figs. 8a, 9a).

Thirty-two analyses were conducted on 14 individual monazite grains in CL718 (Figs. 8b, 9b). Most monazite grains have resorbed grain boundaries and thin, high-Y rim zones that were too narrow for LA-ICP-MS analysis. Zoning is typically simple and concentric with 1–2 core zones overgrown by a thin rim (Fig. 7c), but highly resorbed, patchy cores are locally observed. Most monazites in CL718 host only 1–2 domains of dateable width, so that the chemical signatures and textural relationships between multiple age domains are difficult to assess.

The sample CL831 monazite population is dominated by anhedral grains that typically display complex, patchy zoning, with multiple domains and a number of thin, chemically distinct rims (Fig. 7d,e).
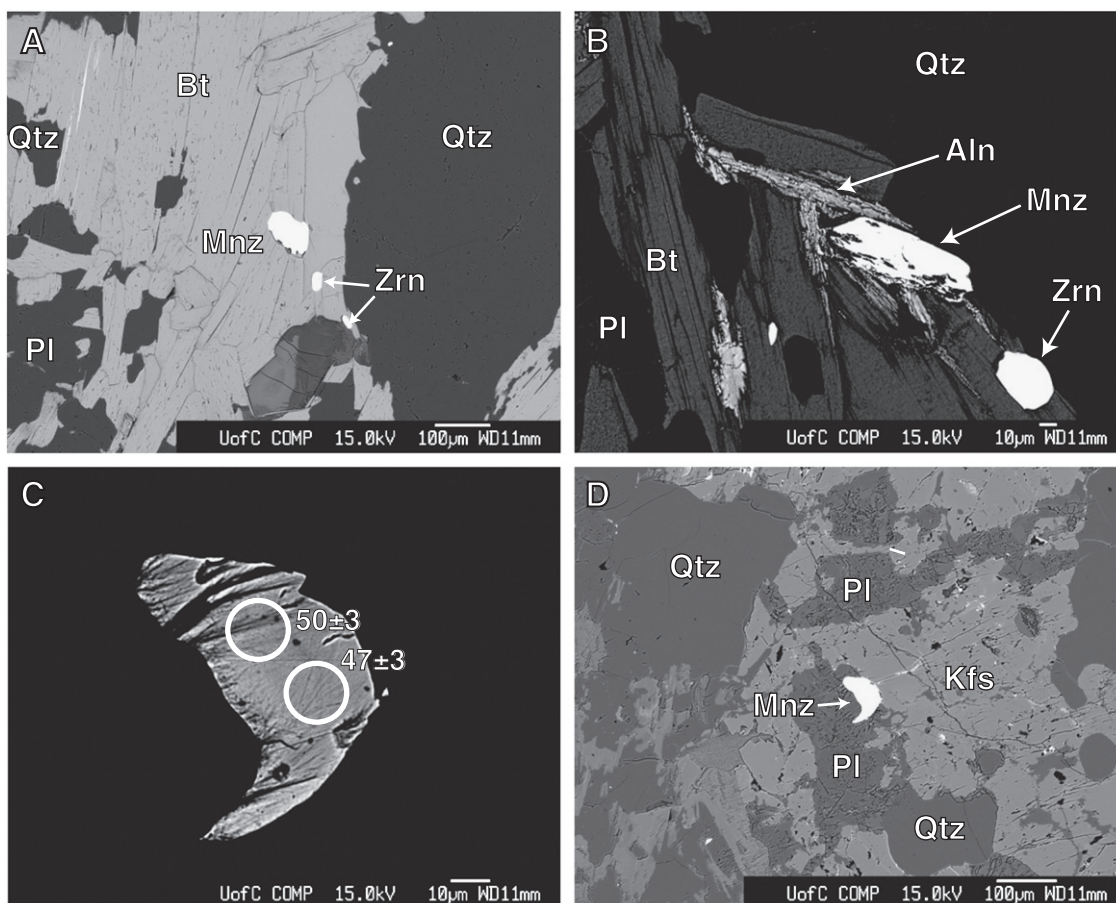
Fig. 6. Monazite in paragneiss leucosomes and bounding biotite selvages. (a) CL931: Monazite inclusion in biotite selvage, with small zircon inclusions nearby. (b) Late allanite growth in biotite selvage. Allanite replaces monazite and is localized along biotite {001} cleavage planes. (c) CL592: Unzoned Generation 7, ~50 Ma monazite grain in leucosome. (d) CL592: Textural location of unzoned monazite in Fig. 6c, as partial inclusion within plagioclase and in contact with K-feldspar within stromatic leucosome.

The relatively simple concentric zoning and core–rim relationships observed in other samples are generally absent from sample CL831, and the ambiguous growth relationships between patchy internal zones makes interpretation difficult (e.g. Fig. 7e). The long axis of most monazites in melanosome layers is oriented in the plane of the foliation, in contrast to monazites observed in undeformed Kfs + Qtz-rich leucosomes where grain orientations are highly variable. Forty-two single-domain spots were analysed on 17 individual grains (Figs. 8c, 9c; Appendix B).

The monazite population in sample CL931 is predominantly composed of blocky, subhedral to euhedral monazite grains, whose long axes are oriented parallel to the foliation. The exceptions to this are monazites in biotite selvages, which have random orientations. Monazite, in addition to zircon and late allanite, is found in greater abundance within these selvages than elsewhere in the thin section. Monazite in CL931 typically has only 2 zones, a core and a rim. There are six monazite populations in sample CL931 (Table 1), based on 26 analyses on 13 grains (Figs. 8d, 9d), with a maximum of three age domains observed in a single grain.

3.2.2. Summary GFC monazite age results

A probability–density compilation diagram of all common Pb-corrected GFC monazite ages is presented in Fig. 10. The U–Pb results of Laberge and Pattison (2007) are shown for comparison. Weighted mean $^{206}Pb/^{238}U$ ages were determined for seven distinct monazite populations (Fig. 10; Table 1) ranging in age from the Late Jurassic to Early Eocene. A box plot of the distribution of ages within those populations is shown in Fig. 11. Each population does not necessarily indicate an individual metamorphic event, but instead merely represents a period of monazite growth. More than one growth episode

is possible in a single metamorphic event, and monazite growth is not restricted to peak conditions (e.g. Janots et al., 2008; Spear, 2010; Wing et al., 2003). Hermann and Rubatto (2003) showed that even at relatively dry, granulite facies conditions a single metamorphic event can yield at least three different age populations reflecting different points on a prograde path.

Monazite Generation 1 (n = 12) comprises irregular, patchy core domains in monazites within samples CL592 and CL831, and has a weighted mean $^{206}Pb/^{238}U$ age of 144.9 ± 2.5 Ma (MSWD = 1.1) (Table 1). Where mapped, it shows enrichment in Ce, La, and U relative to later growth domains. Generation 2 (n = 7) has a weighted mean $^{206}Pb/^{238}U$ age of 126.7 ± 3.4 Ma (MSWD = 0.9) and is observed as resorbed, irregular core domains in CL592 and CL831 that lie rimward of Generation 1 where both populations are present. No Generation 2 domains were chemically mapped during the initial X-ray mapping of this study, but the two generations are clearly distinguishable in BSE images.

Monazite Generation 3 (n = 33) has a weighted mean $^{206}Pb/^{238}U$ age of 95.2 ± 1.0 Ma (MSWD = 1.1) and was recorded in all analysed samples. Generation 3 domains comprise resorbed, anhedral core zones, as well as intermediate zones between Generation 1 & 2 cores and younger rim domains. They are enriched in Y but depleted in Nd, Ce, Th, & La relative to Generation 4 domains which lie immediately rimward. Two chemically and temporally distinct "subgenerations" are evident in some monazite grains: Generation 3a (99–96 Ma) is enriched in Ca & Th relative to Generation 3b (96–92 Ma), which has higher concentrations of Nd, Ce, La & Y. Generation 4 (n = 23) has a weighted mean $^{206}Pb/^{238}U$ age of 84.4 ± 1.1 Ma (MSWD = 1.4) and is observed as 1) small intermediate annulus domains (Appendix A.b); 2) larger intermediate domains (Appendix A.a); 3) subhedral to anhedral
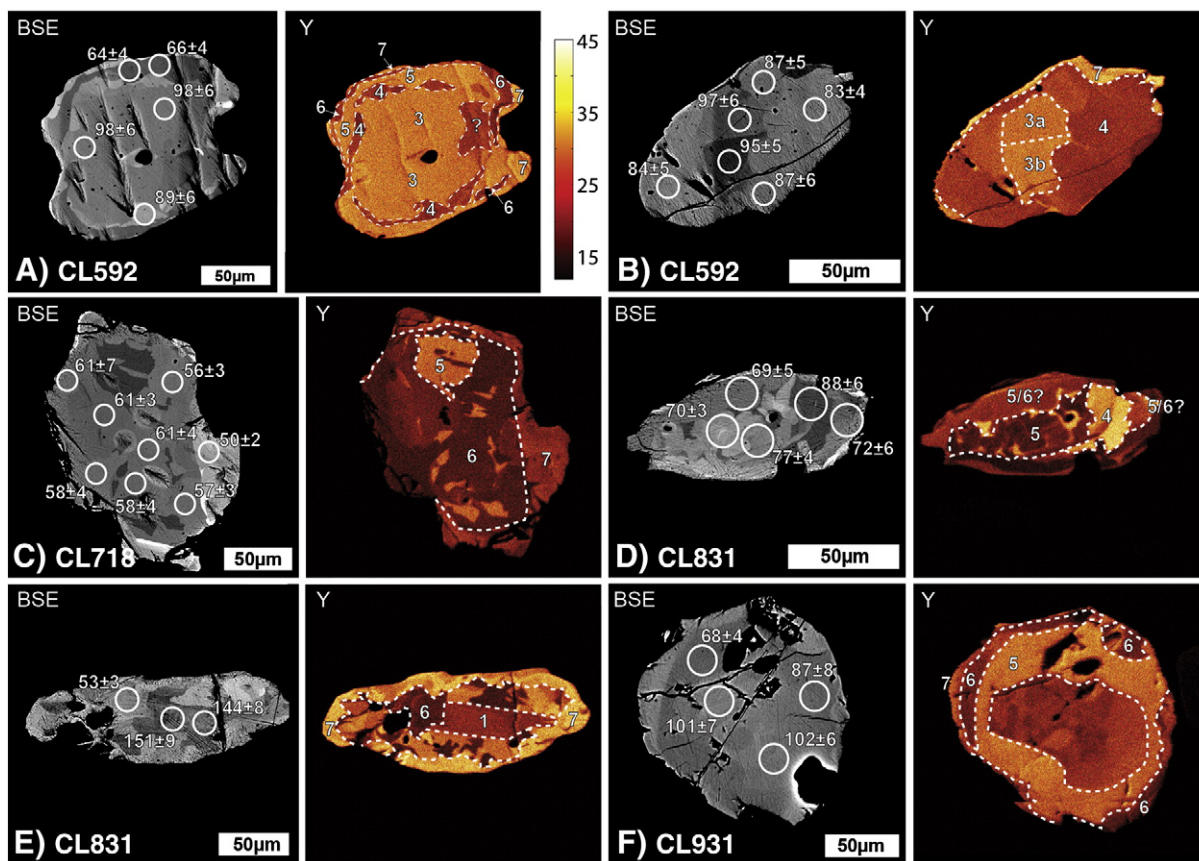
Fig. 7. Electron microprobe yttrium X-ray chemical maps in representative samples from the Grand Forks complex, with accompanying BSE images showing the location of analysis spots and associated corrected U–Pb ages. Microprobe operating conditions and dwell times were held constant for all maps and the color bar (shown in panel a) represent raw counts for yttrium. Interpreted zoning is shown superimposed on yttrium maps. Note the common occurrence of high-Y rims immediately rimward of low-Y, ~60 Ma zones (panels a,c,f). See text for discussion.

core zones; and 4) rare unzoned monazite in melanosomes. Compared to the younger Generation 5 monazite that locally bounds it, Generation 4 monazite has lower Y but higher U concentrations.

Generation 5 (n = 19) has a weighted mean $^{206}Pb/^{238}U$ age of 67.8 ± 0.9 Ma (MSWD = 3.2). Observed in monazite from all samples, Generation 5 domains comprise the resorbed, irregular core zones of smaller monazites and intermediate zones of larger monazites. Monazite grains with Generation 4 cores and Generation 5 rims are locally observed, as are rare, unzoned Generation 5 monazites in melanosome layers. Generation 5 domains are enriched in Y yet depleted in La, Ce, Ca, Th & Nd relative to Generation 4 (Appendix A.b)

Generation 6 (n = 34) is the dominant monazite population in the four analyzed paragneiss samples, with a weighted mean $^{206}Pb/^{238}U$ age of 58.6 ± 0.6 Ma (MSWD = 1.9). Generation 6 domains comprise intermediate zones and locally rims on large monazites. Intermediate zones of this generation are typically highly resorbed with Generation 7 overgrowth rims. In small monazites, Generation 6 domains comprise homogenous core zones in monazites from all textural locations. Rare unzoned Generation 6 monazite is observed in both leucosome and melanosome. In comparison with chemical signatures from rimward Generation 7 domains, Generation 6 domains show significant Y & Th depletion, with variable enrichment in Ca, Ce, La, and U (Appendix A.b,c,f).

Generation 7 (n = 13) is characterized by high-Y rims on the edges of most monazite grains (Fig. 7), and has a weighted mean $^{206}Pb/^{238}U$ age of 49.9 ± 1.0 Ma (MSWD = 2.4). The low number of analyses in this population does not reflect the abundance of these rims, as the

width of most rims is less than the 16 μm spot size. In addition to the high-Y signature, Generation 7 monazite shows enrichment in Th relative to older domains. Yttrium concentrations of Generation 7 domains are similar to those in Generations 3 & 5 domains, but markedly higher than in Generation 6 domains (Appendix A.b,f).

3.2.3. Statistical determination of age populations

An alternate way of identifying GFC monazite age populations is through statistical unmixing of the complete dataset using ISOPLOT (Ludwig, 2003). Spot analyses including multiple domains were again removed from the dataset. Unmixing of six components yields the following age populations, with a relative misfit of 0.129: 1) 144.6 ± 2.7 Ma; 2) 122.6 ± 3.8 Ma; 3) 95.05 ± 1.3 Ma; 4) 84.2 ± 2.6 Ma; 5) 65.5 ± 2.8 Ma and 6) 55.7 ± 1.2 Ma. These ages closely coincide with the weighted mean $^{206}Pb/^{238}U$ ages calculated above.

3.3. Thermodynamic modeling of monazite growth

Most monazite grains from the GFC contain a patchwork of chemical zones, with truncation of earlier zones and juxtaposition of different chemical domains. These chemical patterns are similar to those of previous studies (Gibson et al., 2004; Parrish, 1990; Pyle and Spear, 1999, 2003; Pyle et al., 2001; Williams et al., 1999). In some of these studies, distinct age domains were linked with specific chemical zones (Foster et al., 2002; Gibson et al., 2004). The most commonly used chemical indicator is Y concentration, which is strongly controlled by garnet growth and breakdown (Foster et al., 2000; Pyle
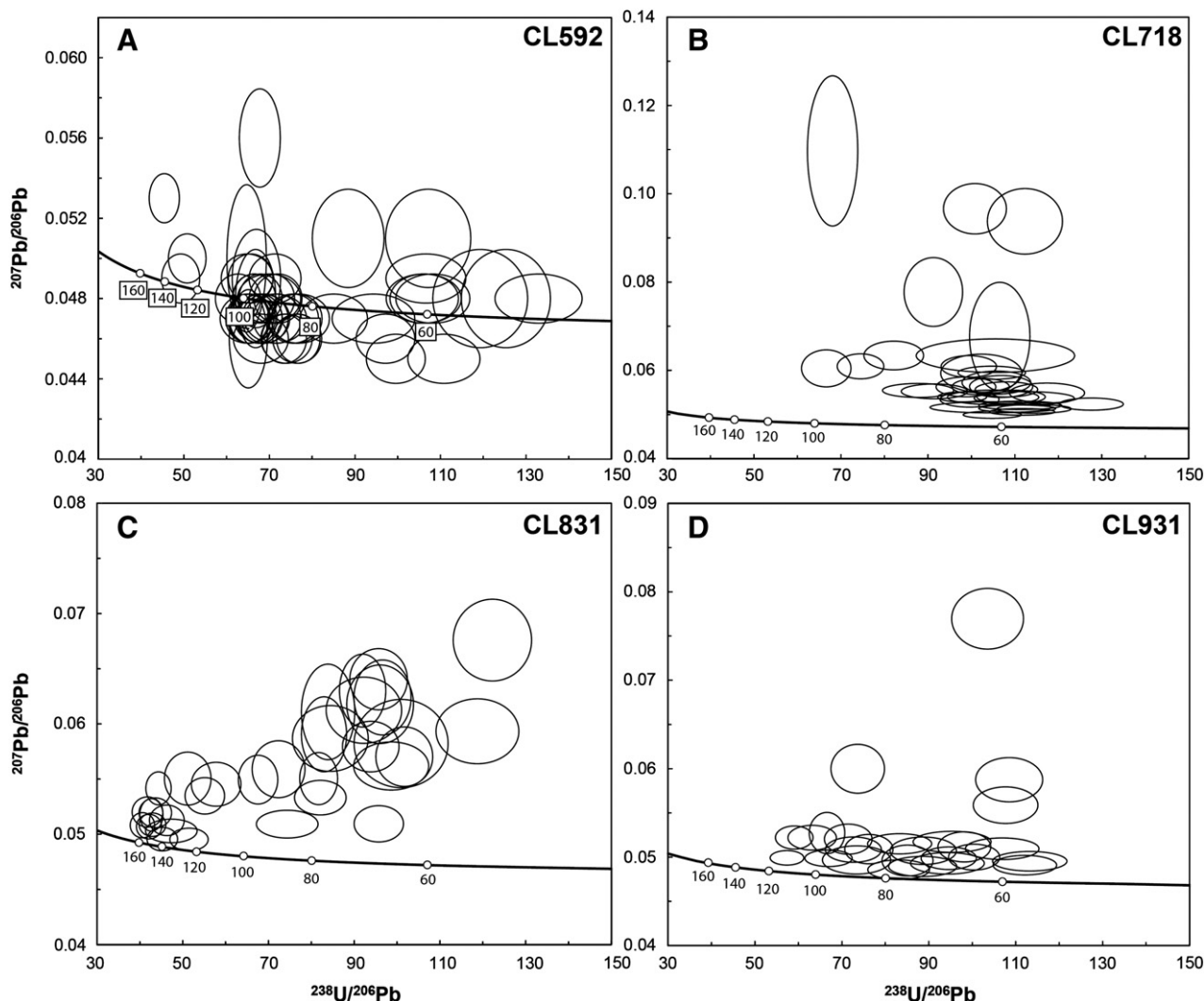
Fig. 8. Tera–Wasserburg U–Pb concordia plots for monazite samples from the GFC. Input errors were 2σ. See text for details.

and Spear, 1999). Because garnet can accommodate several thousand ppm Y, garnet growth and subsequent Y sequestration has been shown to have a strong effect on monazite growth and composition (e.g. Foster et al., 2000; Pyle and Spear, 2000; Zhu and O'Nions, 1999).

Twelve-component MnNCKFMASHPYCe (MnO-Na$_2$O-CaO-K$_2$O-FeO-MgO-Al$_2$O$_3$-SiO$_2$-H$_2$O-P$_2$O$_5$-Y$_2$O$_3$-Ce$_2$O$_3$) isochemical phase diagram sections were constructed for each of the 4 dated samples to examine the relationships between monazite, garnet, and the melt phase. A representative section for sample CL592 is shown in Fig. 12. Phase diagram sections were constructed from bulk rock XRF data (Appendix C) obtained at one of two facilities: 1) McGill University, using a Philips PW2440 4 kW spectrometer system, or 2) Washington State University using a ThermoARL Advant'XP spectrometer system. Isochemical phase diagram sections were constructed using the Gibbs free energy minimization software Theriak-Domino (de Capitani and Brown, 1987; de Capitani and Petrakakis, 2010), using the thermodynamic database presented in Spear and Pyle (2010). Fixed whole rock H$_2$O contents for modeling at suprasolidus conditions were calculated based on the total amount of H$_2$O contained in hydrous phases immediately down-temperature of the wet solidus. This method of determining whole rock H$_2$O content is reasonable due to negligible porosity in high grade metapelites at the P–T conditions of relevance to this study. This calculation was made at 5.8 kbar, the pressure of peak metamorphism in the GFC calculated by

Laberge and Pattison (2007) and Cubley and Pattison (2009). Any H$_2$O generated by suprasolidus dehydration reactions is assumed to have dissolved in the melt phase (dehydration melting) and the modeling assumes that the rock was closed to the loss of melt and therefore to the loss of H$_2$O. The subsolidus portion of the diagram was constructed with an H$_2$O fluid phase in excess. Because the temperature conditions of interest (~600–900 °C) lie above the terminal stability of allanite at low pressures (e.g. Spear, 2010; Tomkins and Pattison, 2007), allanite was not included in the thermodynamic database. Whole-section chemical mapping of Ca, Ce, P, and Y in CL592 revealed only trace apatite and no xenotime.

In the isochemical phase diagram section for CL592 (Fig. 12), the assemblage stability fields corresponding to the peak metamorphic (Sil + Grt + Bt + Kfs + Pl + Qtz + Ilm) and low pressure matrix mineral assemblage (Grt + Bt + Crd + Kfs + Pl + Qtz + Ilm) are outlined in the dashed lines. Metamorphic P–T estimates for the peak metamorphic and low-pressure coronal decompression assemblages in the GFC by Cubley and Pattison (in press) are shown with associated error estimates.

Mineral isopleth diagrams were constructed for the number of moles of monazite (Fig. 13a), moles of garnet (Fig. 13c), and moles of melt (Fig. 13e) in the sample, as well as Y# (Y/(Y + Ce)) in monazite (Fig. 13b), moles of Y-endmember garnet (YAG; n = X$_Y^{Grt}$*moles Grt)
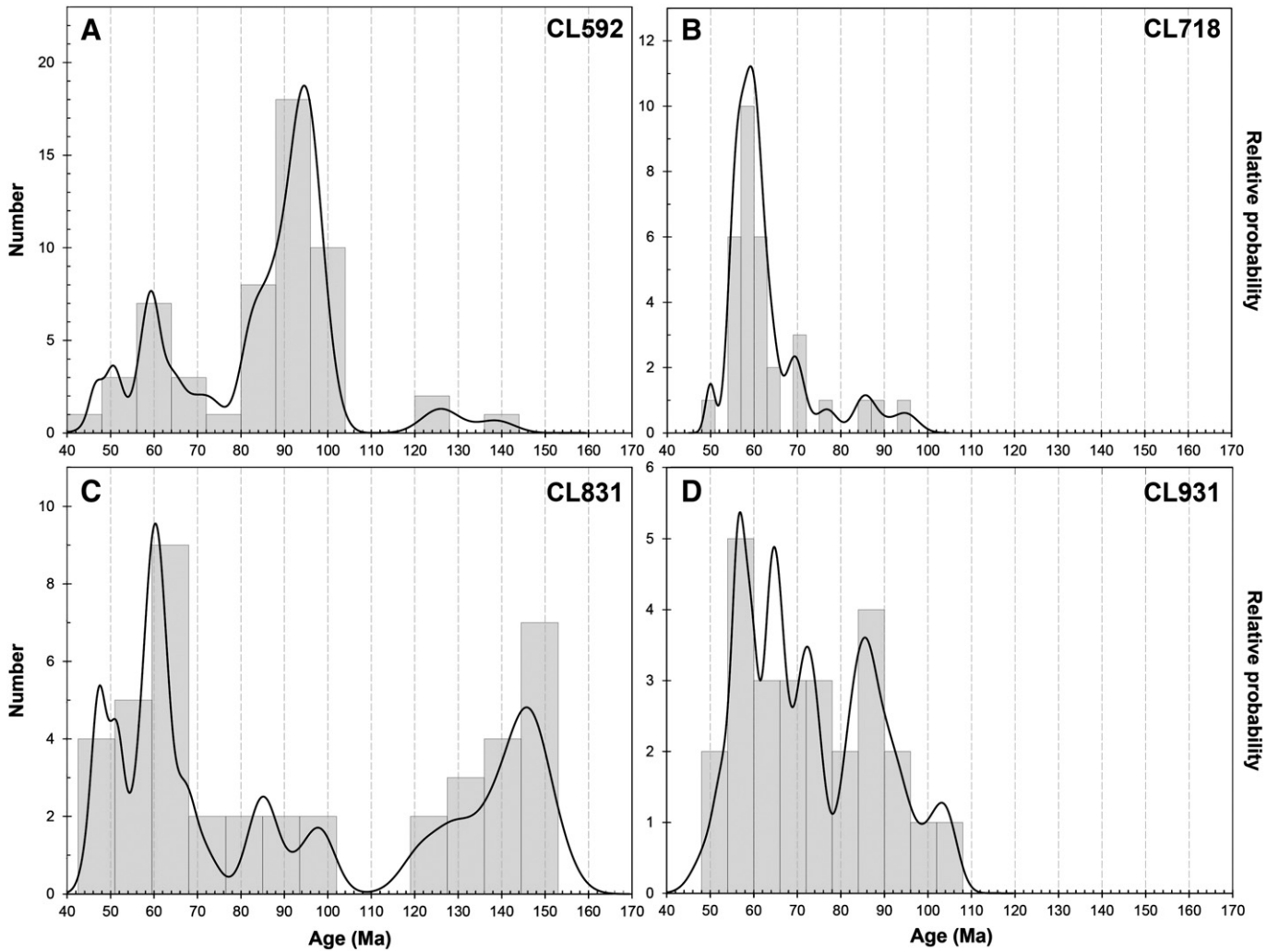
Fig. 9. Probability–density diagrams for common Pb-corrected U–Pb ages in monazite samples from the Grand Forks complex. Input errors were 2σ.

Fig. 10. Summary of common Pb-corrected monazite ages from four GFC paragneiss samples. Ages shown are weighted mean [206]Pb/[238]U ages for populations determined by relative chemical composition and textural context, as well as age. Errors are reported at 2σ. For comparison purposes, the U–Pb monazite data of Laberge and Pattison (2007) are shown (dashed line). See text for discussion.

Table 1
Petrographic and chemical characteristics of GFC monazite populations.

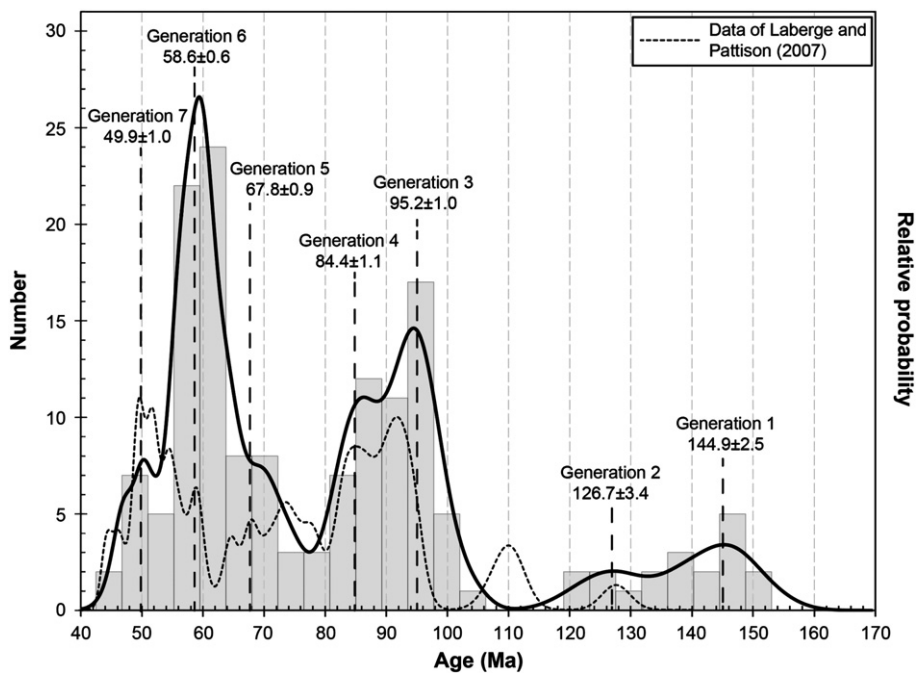| Number of analyses	Age (2σ)	MSWD	CL592	CL718	CL831	CL931	Textural location within monazite grain	Relative chemical signature	Notes
12	144.9 ± 2.5	1.1	X		X		Irregular, patchy core domains (A.e).	Enriched in Ce, La & U relative to later growth domains (A.e).	
7	126.7 ± 3.4	0.9	X		X		Resorbed, irregular core domains rimward of Gen. 1.	Not mapped, but distinct in BSE from Gen. 1.	Possibly a mixture between two individual Late Cretaceous populations.
33	95.2 ± 1.0	1.1	X	X	X	X	Resorbed, anhedral cores zones (A.a,b); intermediate zones between Gen. 1 & 2 cores and younger rims.	Enriched in Y; depleted in Nd, Ce, Th, and La relative to Gen. 4 (A.a,b). Similar Y to Gen. 5 (A.b).	Two subgenerations (A.a). Older subgeneration (99–96 Ma) is enriched in Ca & Th but depleted in Nd, Ce, La, & Y relative to younger generation (96–92 Ma). Possibility for slightly older 105–100 Ma population with disparate chemical characteristics (A.f).
23	84.4 ± 1.1	1.4	X	X	X	X	Small intermediate annulus zones (A.b) or major intermediate zones (A.a); subhedral to anhedral core zones; single unzoned monazite in melanosome.	Enriched in Th, La, Ce, & Nd, depleted in Ca, U, & Y relative to Generation 3 (A.a). Lower Y than Gen. 5 (A.b). Similar Y, Ce & Nd to Gen. 6, but higher Ca (A.b).	Markedly darker than Gen. 3 & 5 in BSE images.
19	67.8 ± 0.9	3.2	X	X	X	X	Resorbed, irregular core zones (smaller monazites) and intermediate zones (larger monazites; (A.f)); locally thick rims on Gen. 4 cores; rare unzoned, euhedral grains in melanosome.	Enriched in Y, depleted in La, Ce, Ca, Th & Nd relative to Gen. 4.; Enrichment in Y & Th relative to Gen. 6 (A.f).	Inconsistent chemical signatures suggest multiple individual growth episodes within (A.d).
34	58.6 ± 0.6	1.9	X	X	X	X	Large monazites – intermediate zones and locally rims, often resorbed with Gen. 7 overgrowth rims (A.b,c, f). Small monazites – subhedral to anhedral homogenous core domains in leucosome, melanosome, and selvage monazites. Rare unzoned Gen. 6 monazite observed in both leucosome and melanosome.	Significant Y & Th depletion, variable Ce, Ca, La & U enrichment relative to Gen. 7 rims. (A.b,c,f).	
13	49.9 ± 1.0	2.4	X	X	X	X	Thin rims on nearly all grains (A.a, b); homogenous unzoned grains in leucosomes (Fig. 6c)	Strong enrichment in Y, Th, Ca and depletion in Ce, Nd & La relative to Gen 6 (A.b,c,f); consistent enrichment in Y & Th relative to other domains (A.e). Similar Y to Gens. 5, 3 (A.b,f).	Gen. 7 rims common but too thin to analyze (e.g. A.f).

*A.a-f refers to individual monazites within Appendix A.

(Fig. 13d), and the moles of YPO$_4$ in the melt phase (n = X$_{YPO4}^{melt}$ * moles melt) (Fig. 13f). Decreasing the input pressure for the H$_2$O content calculation increases the amount of melt at low-P stability conditions by minor amounts (1.5 kbar reduction leads to 1 mol melt change).

(1) Prograde path and behavior of monazite: Little is known about the prograde P–T path for GFC samples, owing to weak to nonexistent garnet zoning and the lack of dateable monazite inclusions in garnet. Two monazites dated as inclusions in garnet by Laberge and Pattison (2007) revealed a single Late Cretaceous core age (119.3 ± 3.5 Ma) and rim ages ranging between 89 and 78 Ma, suggesting the complex achieved amphibolite facies conditions in the Late Cretaceous. Along a hypothetical clockwise P–T path above the wet solidus but below Ms + Qtz breakdown, monazite breaks down with increasing pressure and temperature (Fig. 13a), concurrent with garnet growth (Fig. 13c) and an increase in the number of moles of the Y-endmember (YAG) (Fig. 13d). Temperature increase along this path also leads to monazite components (Y, Ce) entering the melt phase (Fig. 13f). At the muscovite-quartz breakdown reaction, monazite reaches its terminal stability (Fig. 13a), with released yttrium strongly

partitioning into the melt phase (Fig. 13f). Up-temperature of Ms + Qtz breakdown, yttrium is preferentially taken up by garnet (Fig. 13c,d) with a concurrent decrease of Y in the melt (Fig. 13f). Regardless of the prograde metamorphic path, no monazite age population in sample CL592 represents peak metamorphism, because monazite is predicted to be unstable at peak conditions (Fig. 13a). This conclusion will hold true even if some melt escaped from the reacting system due to the strong partitioning of Y and/or Ce into the melt phase and garnet during prograde heating, which would reduce the potential for new monazite growth even further. The same result was obtained for the other samples in this study.

(2) High-T decompression and monazite growth: High-temperature decompression in the GFC from peak P–T conditions to low-P coronal conditions is predicted to lead to the growth of new monazite (Fig. 13a). The molar abundance of garnet shows a small increase upon crossing the MnNCKFMASH Bt-dehydration reaction Bt + Sil + Qtz = Crd + Grt + Kfs + melt, but then decreases with decompression through the Grt + Crd field (Fig. 13c). The number of moles of YAG also decreases in the Grt + Crd field, and this release of yttrium is partially taken up
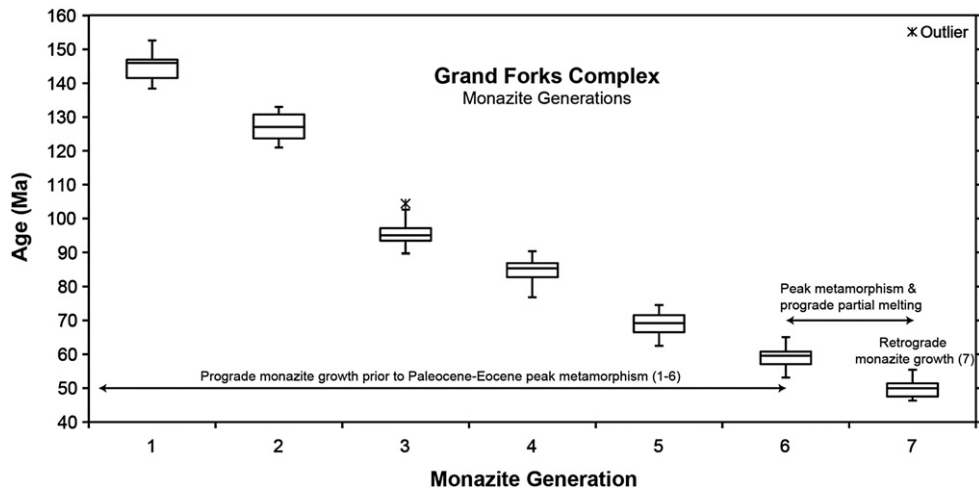
Fig. 11. Box-and-whisker plot of the distribution of the seven monazite populations delineated for the Grand Forks complex.

by an increase in YPO$_4$ in the melt phase (Fig. 13f), and by new monazite growth. Subsequent cooling from this low-P assemblage to the wet-solidus leads to further growth of monazite at the expense of melt and garnet (Fig. 13b,d,f). The Y# of monazite is predicted to increase during this cooling interval.

Despite the above predictions, monazite is present in the peak assemblage and records ages that predate regional peak metamorphism in the Paleocene to Eocene. Therefore, disequilibrium processes must be considered, in particular relatively low solubility in peraluminous melts (Montel, 1993; Rapp and Watson, 1986) and sluggish reaction kinetics (Kelsey et al., 2008). The combination of these two factors may result in monazite persisting as a metastable phase through suprasolidus conditions (Williams et al., 2007). Partial dissolution of monazite is also possible, and is suggested by discontinuities in zoning in Fig. 7. Whereas partial dissolution of monazite will affect the absolute modal variation of monazite of Fig. 13, it does not affect the major intervals of monazite stability, as revealed by a test in which half the Y and Ce contained within monazite was subtracted from the bulk composition just below the Ms + Qtz-breakdown reaction. A more complete examination of this question is beyond the scope of the paper.
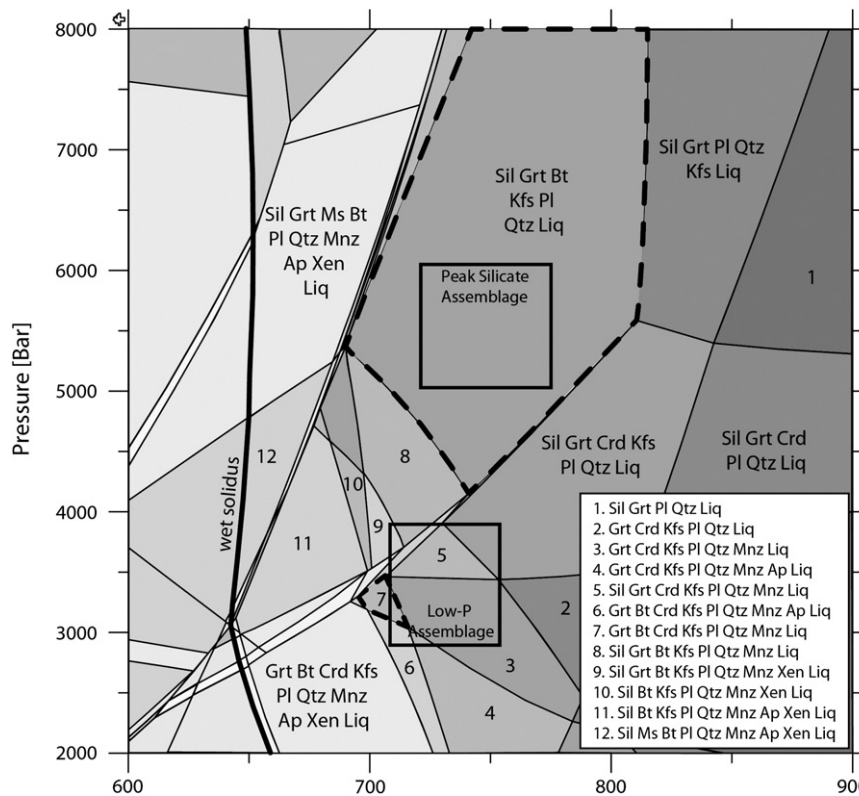

Fig. 12. MnNCKFMASHPYCe isochemical phase diagram section for pelite sample CL592, shaded for variance (darker colors represent greater variance). The assemblage stability fields for the peak metamorphic and low-P decompression assemblage are outlined by the dashed lines, and the P–T estimates from Cubley and Pattison (in press) are shown. Liq = melt.
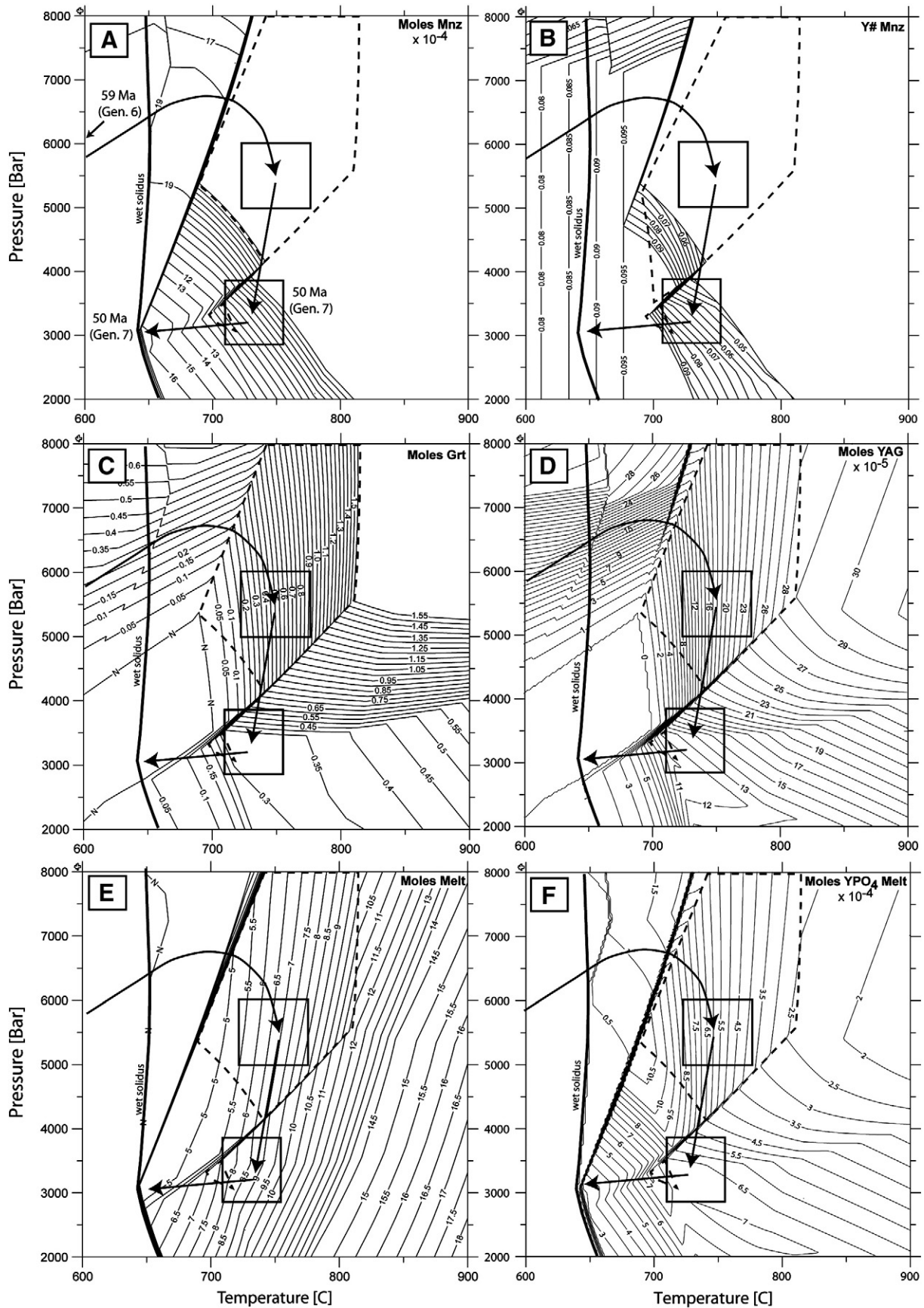
Fig. 13. Mineral abundance and composition isopleths for sample CL592. (a) Isopleth diagram of moles of monazite. (b) Isopleth diagram of Y# in monazite (Y# = Y/(Y + Ce)). (c) Isopleth diagram of moles of garnet. (d) Isopleth diagram of the moles of Y-garnet (YAG). (e) Isopleth diagram of moles of melt. (f) Isopleth diagram of moles of YPO$_4$ in the melt phase. A schematic prograde metamorphic path, calculated decompression path (Cubley and Pattison, in press), and schematic low-P cooling path are shown in each diagram. See text for discussion.

3.4. Monazite discussion and regional comparisons

The Omineca Belt experienced deformation and crustal thickening from the Late Jurassic to Paleocene (Evenchick et al., 2007 and references therin), consistent with the wide spread of GFC monazite ages in Figs. 10 and 11. This protracted metamorphic history was punctuated by 5–6 main periods of metamorphism, deformation and plutonism (Crowley et al., 2000; Evenchick et al., 2007; Parrish, 1995 and references therein). Though the details vary, the ranges are as follows: 170–160 Ma, 145–130, 115–122, 112–110, 100–92, and 75–55. Individual areas in the Cordillera may not have experienced all of the above episodes (Crowley et al., 2000), and the exact timing of each episode varies with geographic location and structural level. The following section examines the driving forces for each episode of monazite growth, be they prograde or retrograde, and provides a comparison of monazite geochronology results from this study with U-Pb data from other core complexes in the composite Shuswap complex (Fig. 14). This comparison is made recognizing that the data represent a range of analytical equipment (e.g. LA-ICP-MS, SIMS), techniques (in situ analysis, crystal separates, depth profiling), analytical protocols, analytical standards and perhaps above all petrological interpretation.

3.4.1. Generations 1 (~145 Ma) & 2 (~127 Ma)

Monazite Generations 1 and 2 fall within a recognized period of Late Jurassic to Early Cretaceous (150–120 Ma) regional metamorphism and magmatism tied to the early compressional stage of the Cordilleran orogeny, interpreted to result from the accretion of the allochthonous Intermontane terrane (Crowley et al., 2000; Currie, 1988; Digel et al., 1998; Evenchick et al., 2007; Monger et al., 1982; Parrish, 1995; Reid, 2003; Scammell, 1993). In a previous study of the Grand Forks complex, Laberge and Pattison (2007) found a single monazite (119 ± 4 Ma) as an inclusion near the core of a large garnet crystal. Similar Early Cretaceous metamorphic monazite ages have been reported for the Aberdeen gneiss complex (Glombick, 2005), the metamorphic cover sequence of Frenchman Cap dome in the northern Monashees (e.g. Crowley et al., 2000; Scammell, 1993), and the Cariboo Mountains (Currie, 1988; Reid, 2003) (Fig. 14).

3.4.2. Generation 3 (~95 Ma)

Generation 3 ages correspond to a second major metamorphic and plutonic episode well-documented throughout the Shuswap complex (e.g. Crowley et al., 2000; Digel et al., 1998; Johnston et al., 2000; Parrish, 1995; Scammell, 1993; Sevigny et al., 1989). This episode has been linked to northeast-propagating shortening and thickening following the accretion of the Insular Belt to the Intermontane Belt by mid-Cretaceous time (~100 Ma) (Evenchick et al., 2007; Monger et al., 1982).

The oldest monazite growth ages assigned to Generation 3 in this study (Appendix B) overlap with Generation 2 (104 ± 3 Ma, n = 3) monazites from previous work on the GFC by Laberge and Pattison (2007). Elsewhere in the Shuswap complex, similar metamorphic monazite ages have been reported in the metamorphic cover sequence of Thor-Odin dome in the southern Monashee complex (Johnston et al., 2000), and the cover sequence of Frenchman Cap in the northern Monashees (Crowley et al., 2000; Digel et al., 1998; Scammell, 1993) (Fig. 14).

3.4.3. Generation 4 (~84 Ma)

Monazite grains in Generation 4 of this study fall within the dominant monazite age population of Laberge and Pattison (2007) for the GFC, 84 ± 3 Ma. Monazite growth of this age has been linked to prograde metamorphism and associated anatexis in the northern Monashee complex (Digel et al., 1998), the Valhalla complex (Spear, 2004; Spear and Parrish, 1996) (Fig. 14), and the Okanogan dome (Kruckenberg et al., 2008). Generation 4 ages may represent a late stage of the ~100–92 Ma metamorphic event, or the beginning

stages of the subsequent 72–56 Ma phase of regional metamorphism, below.

3.4.4. Generation 5 (~68 Ma)

Monazite Generations 5 and 6 are linked to prograde burial metamorphism during the final orogenic pulse affecting the Canadian Cordillera, which lasted from the Late Cretaceous to Eocene (~80–50 Ma) (English and Johnston, 2004; Evenchick et al., 2007). Crustal thickening and metamorphism at this time are attributed to a number of mechanisms including retroarc thrusting (Price, 1981) and transpressional collision (Johnston, 2001). No major accretionary event is recorded (English and Johnston, 2004).

Laberge and Pattison (2007) recorded monazite ages from the GFC broadly correlative with Generation 5 in their poorly defined Generation 4 (74–56 Ma). In the cover sequence of the northern Monashees, upper-amphibolite facies metamorphism with associated emplacement of anatectic granitoid bodies has been recorded at this time (Crowley et al., 2000; Digel et al., 1998). Monazite dating of metapelites from the Valhalla complex (Gordon et al., 2008) identified age populations that overlap with Generation 5 and are coeval with Zrn + Mnz ages for the emplacement of granitic pegmatite (Spear and Parrish, 1996) and crystallization of leucosome in gneisses (Parrish, 1990) (Fig. 14).

3.4.5. Generation 6 (~59 Ma)

Generation 6, the dominant age population of this study, was somewhat surprisingly not identified as a significant age population by Laberge and Pattison (2007) (Fig. 10). This ~59 Ma age has been identified throughout the Cordillera by other authors, most of whom have also attributed it to peak prograde metamorphism with associated anatexis. Thermodynamic modeling suggests Generation 6 cannot record peak metamorphism directly (Fig. 13a), as above the Ms + Qtz breakdown reaction monazite is predicted to be unstable and it does not becomes stable again until lower pressures are attained (Fig. 13a). It is therefore interpreted as the last episode of prograde, subsolidus metamorphic monazite growth and provides a lower age constraint on the timing of prograde peak metamorphism and anatexis in the Grand Forks complex. A potential reaction leading to monazite growth on the prograde path involves the subsolidus breakdown of allanite to monazite close to the staurolite and/or kyanite-in boundaries, between ~560 and 610 °C (e.g. Janots et al., 2008; Tomkins and Pattison, 2007; Wing et al., 2003).

In the cover sequence of Frenchman Cap dome in the northern Monashee complex, Paleocene ~60–58 Ma monazite ages have been recorded by Crowley (1997), Parrish and Scammell (1988), Crowley and Parrish (1999), Gibson et al. (1999), and Crowley et al. (2000), among others, whereas similar ages are recorded in the cover sequence of Thor-Odin dome by Johnston et al. (2000). In the core of Thor-Odin dome, Hinchey et al. (2007) proposed prograde peak baric metamorphism with coincident monazite and zircon ages at ~56 Ma, synchronous with leucosome crystallization ages from Vanderhaeghe et al. (1999), Teyssier et al. (2005), and Hinchey et al. (2006). Peak prograde metamorphic monazite growth in the Valhalla complex at ~60 Ma is recorded by Spear and Parrish (1996), Spear (2004), and Gordon et al. (2008), coincident with zircon ages from crystallized leucosome in gneisses (Gordon et al., 2008) and the overlying Ladybird granitic suite (Parrish et al., 1988). In the Okanogan dome, Kruckenberg et al. (2008) recorded 61–58 Ma ages in granitic leucosome in metatexite, attributing these to anatexis in the host migmatites, whereas Glombick et al. (2006) recorded similar U–Pb titanite ages from diorite gneiss in the Aberdeen gneiss complex.

3.4.6. Generation 7 (~50 Ma)

Early Eocene zircon and monazite ages in other core complexes of the southern Cordillera have been attributed to complex exhumation and melt crystallization, linked to the onset of regional extension in
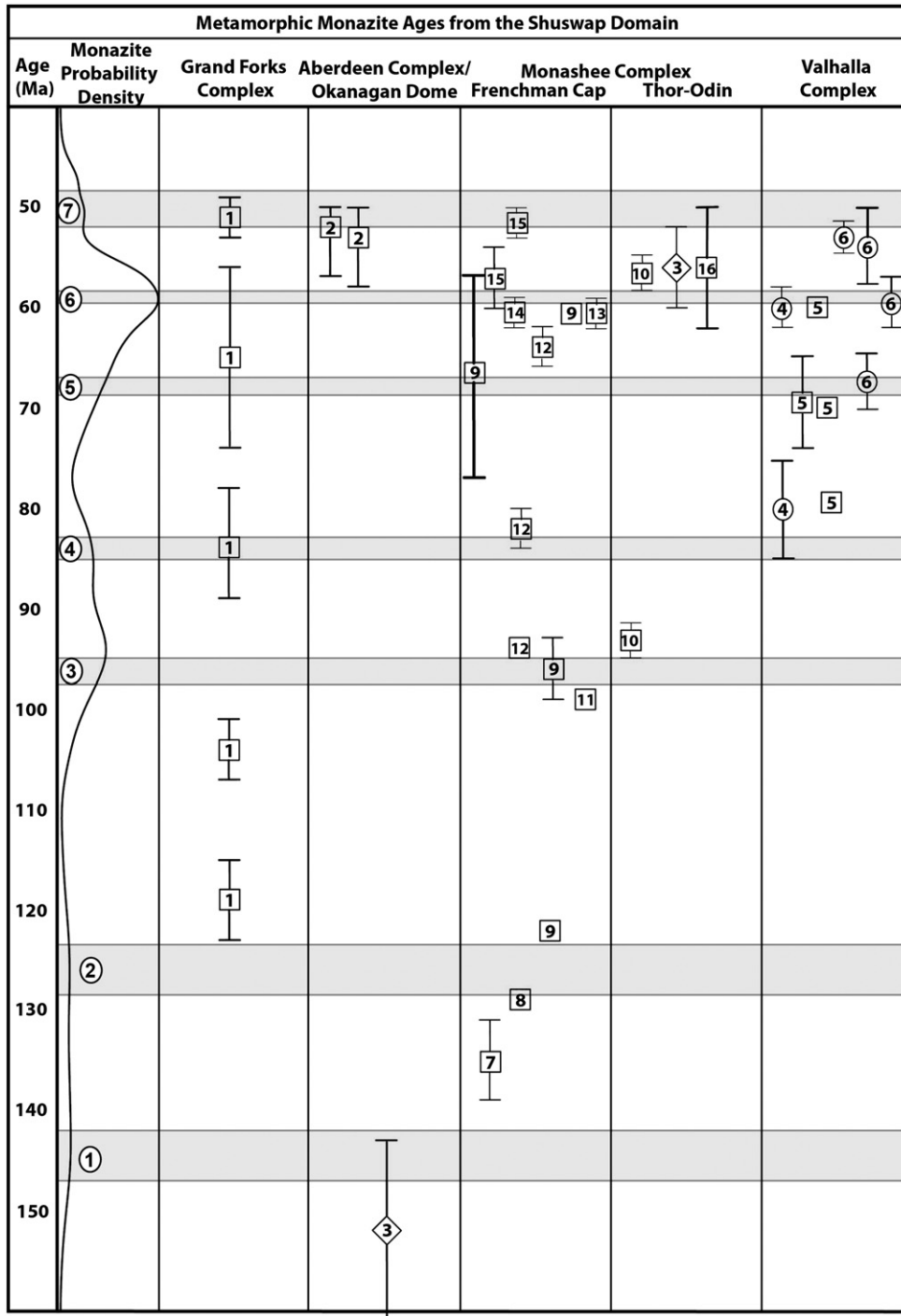
Fig. 14. Comparison plot of metamorphic monazite ages from this study with those reported from other core complexes and cover gneisses of the Shuswap domain. Probability–density plot for metamorphic monazite ages from this study is shown on the left, with gray bands representing the seven growth generations. Results from the following regional studies are shown: (1) Laberge and Pattison, 2007; (2) Kruckenberg et al., 2008; (3) Glombick, 2005; (4) Spear, 2004; (5) Spear and Parrish, 1996; (6) Gordon et al., 2008; (7) Currie, 1988; (8) Sevigny, unpublished data 1992; (9) Crowley et al., 2000; (10) Johnston et al., 2000; (11) Scammell, 1993; (12) Digel et al., 1998; (13) Parrish and Scammell, 1988; (14) Gibson et al., 1999; (15) Crowley and Parrish, 1999; (16) Hinchey et al., 2007; (17) Reid, 2003.

the southern Cordillera at ~55–52 Ma (Parrish et al., 1988; Teyssier et al., 2005; Vanderhaeghe and Teyssier, 2001; Vanderhaeghe et al., 1999). In contrast, a 51 ± 2 Ma monazite population identified in the Grand Forks complex by Laberge and Pattison (2007) was attributed to thermal and/or fluid recrystallization due to the emplacement of the Coryell Batholith in the hanging wall of the Granby fault. Difficulties with this interpretation include: (1) the interpretation of the Coryell Batholith as a cool, epizonal alkali intrusion with a lack of

significant contact metamorphism (Stinson, 1995); 2) the lack of alkalic Coryell intrusives within the GFC itself (Fig. 2); and 3) the presence of 52–50 Ma rims on monazite inclusions in silicate phases, far from grain boundaries and possible hydrothermal fluid flow. We thus interpret Generation 7 monazite to have grown during high-temperature decompression of the GFC and subsequent rapid cooling to subsolidus temperatures (~650 °C). Rapid cooling following decompression is suggested because monazites in both crystallized leucosome (~650 °C)

and high-temperature coronal textures (~735 °C) record ~52–50 Ma ages.

Our interpretation is supported by 1) unzoned Generation 7 monazite grains in leucosome layers (Fig. 6c,d), interpreted to represent final crystallization of anatectic melt at the wet solidus, and 2) the Y-rich composition of Generation 7 monazite domains, consistent with garnet resorption and Y-release during decompression and subsequent cooling (Fig. 13c,e). High-Y monazite rims attributed to garnet breakdown during decompression and cooling have been documented elsewhere by Foster et al. (2002), Gibson et al. (2004), and others. Melanosome monazites contained as inclusions within Crd + Ilm + Spl ± Rt and Crd + Qtz coronal decompression textures (Fig. 5) commonly have Generation 7 monazite rims, suggesting that the decompression textures that surround this monazite growth are coeval with or postdate 49.9 ± 1.0 Ma.

In the Okanogan dome, Kruckenberg et al. (2008) recorded zircon and monazite ages down to 49 Ma, with mean ages from diatexite at 51.1 ± 1.0 Ma, interpreted to represent leucosome crystallization. North in the Aberdeen complex, Glombick et al. (2006) concluded that Paleocene to Early Eocene metamorphism (Generation 6 of this study) was closely followed by rapid exhumation and cooling, with zircon rims recording crystallization ages down to ca. 51 Ma. Nearby work by Brown (2010) recorded U–Pb zircon ages of 53–50 Ma from leucocratic layers in migmatitic gneisses.

In the cover sequence of Frenchman Cap dome, Crowley and Parrish (1999) recorded monazite ages correlative with both GFC Generations 6 & 7, whereas in the basement core of the culmination, only 52–50 Ma Generation 7 ages were recorded. In the structurally higher Thor-Odin dome, monazite dating by Hinchey et al. (2007, 2006) recorded near-isothermal decompression and anatexis occurring in the interval ~54–51 Ma, with a cessation of age dates at ~50 Ma. In the Valhalla complex, Gordon et al. (2009, 2008) also reported monazite and zircon ages as young as ~50 Ma.

In combination, Monazite Generations 6 & 7 constrain peak metamorphism in the Grand Forks complex to between 58.6 ± 0.6 Ma and 49.9 ± 1.0 Ma. This age bracket for peak metamorphism is ~26–34 Ma younger than that proposed by Laberge and Pattison (2007).

4. U–Pb zircon constraints on the timing of deformation and exhumation

The monazite data in this study record polyphase metamorphism in metasedimentary units of the GFC. U–Pb zircon constraints from deformed and post-kinematic intrusive rocks help resolve the timing of deformation and exhumation of the GFC relative to those metamorphic events. Zircons were analyzed in this study from four igneous bodies. Two samples were collected from the Grand Forks complex and two were taken from the hanging wall of the Kettle River fault (KRF) (Figs. 2, 15).

4.1. Zircon analytical procedures

Zircon grains were separated from four rock samples using standard crushing, washing, heavy liquid (Sp. Gr. 2.96 and 3.3), and paramagnetic procedures. Hand selected zircon grains were placed onto double-sided tape, mounted in epoxy together with chips of the Temora reference zircons (Black et al., 2003), sectioned approximately in half, and polished. Reflected and transmitted light photomicrographs as well as cathodoluminescence (CL) Scanning Electron Microscope (SEM) images (Fig. 16) were taken for all zircons. The CL images were used to identify the internal structures of the sectioned grains and to ensure that the ~20 μm SHRIMP spots were wholly within a single age component within the sectioned grains.

The U-Th-Pb analyses were performed using SHRIMP II at the Research School of Earth Sciences, The Australian National University, Canberra, Australia following procedures given in Williams (1998, and references therein). Each analysis consisted of 6 scans through the mass range, with the Temora reference zircon grains analyzed for every three unknown analyses. The data were reduced using the SQUID Excel Macro of Ludwig (2001). The Pb/U ratios were normalized relative to a value of 0.0668 for the Temora reference zircon, equivalent to an age of 417 Ma (Black et al., 2003). Uncertainty in the U–Pb calibration was 0.37% for the SHRIMP II session.

Uncertainties given for individual analyses (ratios and ages) are at the one sigma level (Appendix D) with correction for common Pb made using the measured $^{238}U/^{206}Pb$ and $^{207}Pb/^{206}Pb$ ratios, following Tera and Wasserburg (1972) and Williams (1998). Tera and Wasserburg (1972) concordia plots (Fig. 17), probability–density plots with stacked histograms (Fig. 18) and weighted mean $^{206}Pb/^{238}U$ age calculations were carried out using either ISOPLOT or ISOPLOT/EX (Ludwig, 2003). Weighted mean $^{206}Pb/^{238}U$ ages were calculated and uncertainties reported at the 95% confidence level.

4.2. Grand Forks complex U–Pb zircon samples

4.2.1. Undeformed quartz monzonite (CL891)

Numerous undeformed granite to quartz monzonite intrusive bodies are exposed along Highway 3 between Christina Lake and Grand Forks, B.C. (Fig. 2). These granitoids crosscut ductilely deformed rocks of the Grand Forks complex, postdating local high-strain shear zones and the major folding episodes observed in the complex (F_{3a} & F_{3b} of Cubley and Pattison, in press) (Figs. 4c, 15a,b). The intrusive bodies are in turn cut by steeply dipping mafic dikes that are similarly undeformed. On the margins of the GFC, these post-ductile-deformation granitoids are brecciated in the fault zones of the brittle Granby and Kettle River faults (Fig. 4g) (Cubley and Pattison, 2009, in press; Laberge and Pattison, 2007; Preto, 1970; Rhodes and Cheney, 1981). An age of this intrusive suite thus provides 1) an upper age limit on the timing of latest ductile deformation in high-strain shear zones, 2) an upper age limit on major folding in the complex, 3) a lower age limit on the timing of brittle extension on the KRF and GF, and 4) a lower age limit on the emplacement of late mafic dikes.

Numerous authors have correlated these intrusives with the composite Okanagan Batholith, thus assigning them a Jurassic to Cretaceous age younger than the Middle Jurassic Nelson suite intrusives found in the hanging walls of the Granby and Kettle River faults (Höy and Jackaman, 2005b; Little, 1957; Tempelman-Kluit, 1989). However, Laberge (2005) speculated that the granitoids might be Eocene in age, based on mineralogical, textural, and geochemical similarities to Eocene intrusives of the Herron Creek suite of the Colville Batholith in northeastern Washington (Holder and Holder, 1988), dated to 51.3 ± 0.1 Ma (U–Pb zircon) (Wooden and Box, 1996).

Quartz monzonite sample CL891 is located in the center of the GFC structural dome (Fig. 2), and truncates high-strain fabrics in surrounding orthogneisses (Fig. 15a,b). Zircon grains range in size from 60 × 60 μm to 120 × 400 μm, and typically have euhedral grain morphologies (Fig. 16a). Bright cores in CL images are often resorbed and anhedral, but rim growth is increasingly euhedral until the outermost rim. This thin rim is variably resorbed and is anhedral in some grains. Twenty-five spots were analyzed from 25 individual grains (Appendix D). Tera–Wasserburg and density–probability diagrams for sample CL891 are shown in Figs. 17a and 18a, respectively. Proterozoic ages are recorded in the cores of two grains (869 ± 13.6 Ma, 1833 ± 23 Ma) and the rim of a third (1017 ± 13 Ma) — these ages have not been included on the above diagrams for better resolution of the younger age populations. Of the younger age fraction, there exist six discrete age populations that temporally coincide with monazite generations described earlier: 156.4 ± 2.9 Ma (n = 1), 95.5 ± 2.0 Ma (MSWD = 3.6, n = 2), 71.4 ± 0.9 Ma (n = 1), 58.9 ± 0.8 Ma (MSWD = 2.6, n = 4), 52.6 ± 0.5 Ma (MSWD = 1.3, n = 8), and 50.0 ± 0.9 Ma (MSWD = 0.5, n = 3). The dominant Early Eocene zircon age

population, 52.6 ± 0.5 Ma, comes mainly from zircon rims, though one core analysis yields this younger age. The youngest age population at 50.0 ± 0.9 Ma is measured entirely from zircon rims. The youngest age is preferred as the age of final igneous crystallization, as crosscutting field relationships indicate that CL891 post-dates CL1162 (51.2 ± 0.6 Ma; see below).
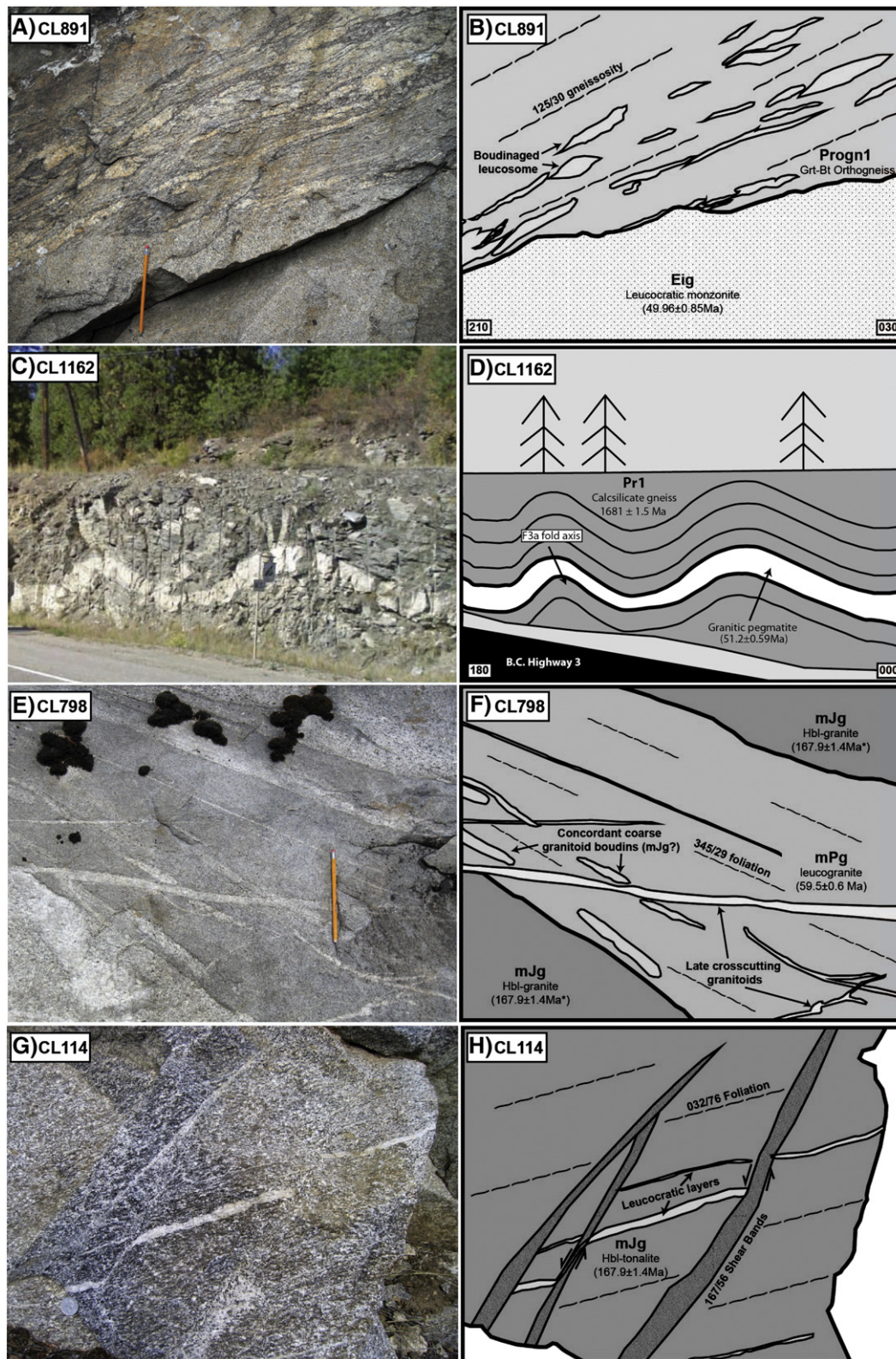

Fig. 15. Field photographs and annotated diagrams for U–Pb zircon geochronology samples. (a,b) Post-tectonic granite (CL891) crosscuts protomylonitic granitic orthogneisses. (c,d) Deformed granitic pegmatite (CL1162) in calc-silicate gneiss. Pegmatite band shows top-to-the-east shearing and subsequent folding by upright F$_{3a}$ folds. U–Pb detrital zircon age for calc-silicate gneiss from Armstrong et al., 1991. (e,f) Leucogranite sample CL798: A band of highly sheared leucogranite is present between layers of coarser grained yet still strongly oriented Hbl-granite of the Jurassic Nelson suite, within the Texas Point shear zone. Late undeformed leucogranitic injections cross-cut ductile fabrics. (g,h) Strongly foliated Nelson-suite Hbl + Bt granodiorite (CL114), cut by cm-scale, high angle ductile shear bands. An asterisk indicates the labeled age is interpreted from another location.
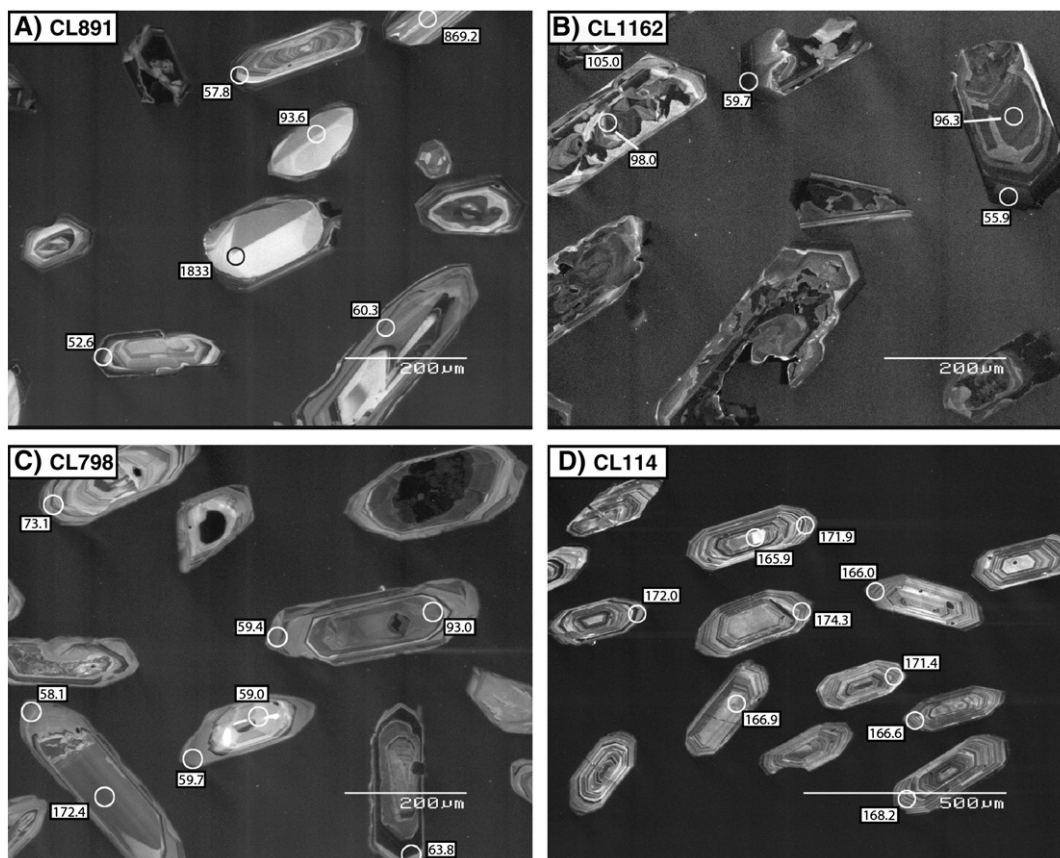
Fig. 16. Representative cathodoluminescence (CL) images for zircon samples from the Grand Forks complex (CL891, CL1162) and Kettle River fault hanging wall (CL114, CL798). SHRIMP ages are in millions of years, without associated 1σ errors (Appendix D).

4.2.2. Deformed leucogranitic pegmatite (CL1162)

On the eastern margin of the GFC south of Christina Lake, layer-parallel granitic to pegmatitic bands in calc-silicate gneisses show evidence for high-temperature ductile shear, namely boudinage and rotation of K-feldspar porphyroclasts along band margins. These textures suggest the pegmatites were emplaced after the development of the predominant S_2 gneissosity (Cubley and Pattison, in press), but prior to the cessation of ductile deformation and top-to-the-east transport. The pegmatite bands have been subsequently folded by F_{3a} folds and truncated by post-kinematic granites (Fig. 4c) correlative with sample CL891, above. A crystallization age for these deformed pegmatite layers provides 1) an upper age constraint of the development of the dominant S_2 gneissosity, 2) a lower age constraint for the timing of final ductile shearing in localized high-strain shear zones in the GFC, and 3) a lower age constraint for the timing of F_{3a} and F_{3b} folding in the GFC.

Leucocratic layers in these migmatites vary from mm-scale stromatic migmatites to pegmatite bands nearly 0.3 m in thickness. Because the pegmatite bands are hosted within calc-silicate gneisses, they are interpreted to represent melt injections, most likely derived from nearby and underlying pelitic gneisses. Sample CL1162 is taken from a Kfs-porphyritic pegmatite band ~20 cm wide (Fig. 15c,d) that shows top-to-the-east shear sense indicators (rotation of K-feldspar porphyroclasts). The pegmatite band is folded by upright F_{3a} folds that plunge shallowly to the east (100–115°). Diffuse, irregular boundaries between the pegmatite band and calc-silicate gneisses suggest the host rocks were still at high temperatures at the time of pegmatite intrusion.

Zircon grains range in size from 40×70 μm to 140×450 μm, with many broken grains (i.e. half grains broken perpendicular to length)

(Fig. 16b). Whereas crystal faces are typically euhedral, the cores of nearly all zircons in this sample are highly resorbed and irregular. Figs. 17b and 18b show Tera–Wasserburg U–Pb concordia and density–probability plots for sample CL1162. Four age populations are evident from 24 spots on 17 individual grains (Appendix D). The oldest U–Pb ages, comprising the dominant zircon age population recorded in CL1162, are inherited Late Cretaceous ages, yielding a weighted mean $^{206}Pb/^{238}U$ age of 97.8 ± 0.6 Ma (MSWD = 2.0, n = 14). These Late Cretaceous ages are recorded both from rims of prismatic grains and the anhedral, resorbed cores of other grains. Two intermediate age populations, 87.3 ± 1.3 Ma (MSWD = 0.05, n = 2) and 55.7 ± 0.8 Ma (MSWD = 0.3, n = 2) are recorded from the rims of some zircons, whereas the dominant rim age, interpreted as final igneous crystallization, is 51.2 ± 0.6 Ma (MSWD = 0.9, n = 4).

4.3. Significance of GFC U–Pb zircon ages

Based on field observations at CL1162, the development of the dominant S_2 gneissosity in the GFC must predate 51.2 ± 0.6 Ma, and high-temperature deformation with top-to-the-east shear must have been ongoing as late as 51.2 ± 0.6 Ma. In combination with observations from post-kinematic granitoid CL891, major F_{3a} and F_{3b} fold episodes are bracketed to a narrow window during or immediately after the final stages of high-temperature exhumation, between 51.2 and 50.0 Ma. All high-T deformation had ceased by the time of the intrusion of undeformed quartz monzonite (CL891) at 50.0 ± 0.9 Ma.

Whereas the post-tectonic ~50 Ma granitoid suite has not been ductilely deformed, it exhibits brittle deformation fabrics in the immediate footwall of the Kettle River and Granby normal faults. This observation implies that the age of latest brittle deformation on the
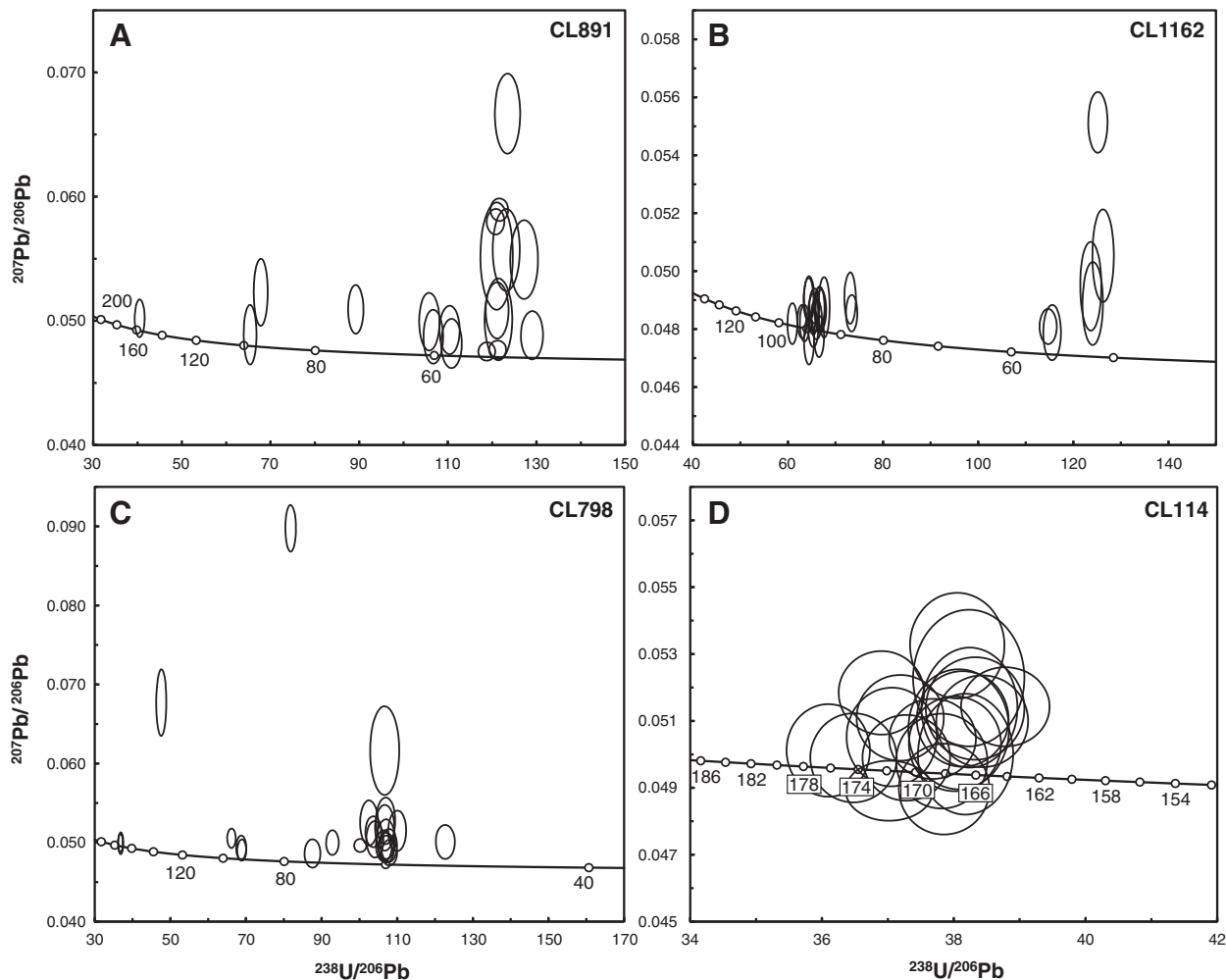
Fig. 17. Tera–Wasserburg U–Pb concordia plots for SHRIMP zircon analyses. Input errors are 1σ.

KRF and GF must postdate 50 Ma. Post-50 Ma movement on these faults is consistent with $^{40}Ar/^{39}Ar$ muscovite ages of ~49 Ma for greenschist facies KRF mylonites in Washington (Berger and Snee, 1992; Mulch et al., 2007). Additionally, it corroborates field constraints on Granby and Kettle River fault deformation that suggest latest movement postdates ~51.1 ± 0.5 Ma, the emplacement of the Coryell intrusive suite (Acton, 1998; Carr and Parkinson, 1989; Cubley and Pattison, in press; Laberge and Pattison, 2007).

The new age for CL891 supports the suggestion of Laberge (2005) that these post-tectonic granitoids are correlative with Eocene intrusives of the Herron Creek suite of the Colville Igneous complex in northeastern Washington (Holder and Holder, 1988; Morris and Hooper, 1997; Morris et al., 2000). The Herron Creek granitoids have been proposed to be the product of decompression melting of the early Proterozoic middle crust during Eocene orogenic collapse and lithospheric extension (Holder and Holder, 1988; Morris and Hooper, 1997; Morris et al., 2000). This explanation is consistent with melt production during high grade metamorphism and decompression of the Grand Forks complex (Cubley and Pattison, in press), and thus a similar origin is tentatively proposed for the ~50 Ma intrusive suite observed in the GFC.

This sequence of events correlates well with what has been found by other studies on late-stage granitoid emplacement during exhumation of the Shuswap domain. In the footwall of the Okanogan Valley fault, Brown (2010) obtained a date of 50.79 ± 0.62 Ma from the Okanogan Batholith, noting that this equigranular granite postdated ductile deformation. Slightly older granitoids (51.8–51.0 Ma) were

foliated with strong fabrics parallel to that in the host gneisses. On the western edge of the Monashee complex, Johnston et al. (2000) dated a post-kinematic, leucocratic aplite/pegmatite dike to 51–50 Ma. On the eastern edge of Thor-Odin dome, Teyssier et al. (2005) reported 55–53 Ma zircon ages from deformed leucosome and pegmatite in host gneisses, whereas crosscutting, undeformed pegmatite was dated at 50.0 ± 0.5 Ma and interpreted to represent the cessation of high-T deformation. To the east of the GFC in the Valhalla complex, Parrish et al. (1988) dated a 51–50 Ma aplite dike that crosscuts mylonitic fabrics of the Gwillim Creek shear zone. In summary, high-temperature, syn-anatectic deformation appears to have ceased by 50 Ma across the southern Shuswap domain.

The emplacement of the late, undeformed mafic dikes common throughout the GFC is now constrained to be younger than ~50 Ma. This is consistent with work by Fyles et al. (1973), who obtained 50–46 Ma $^{40}Ar/^{40}K$ ages for lamprophyre dikes near Rossland, B.C. In the Monashee complex, Adams et al. (2005) obtained a ca. 48 Ma $^{40}Ar/^{39}Ar$ age for a late lamprophyre dike in Thor-Odin dome.

4.4. Kettle River fault hanging wall U–Pb zircon samples

4.4.1. Deformed biotite leucogranite (CL798)

Northeast of Christina Lake, previous mapping identified Jurassic to Cretaceous biotite granites and granodiorites (JKg of Höy and Jackaman, 2005b) spatially associated with Middle Jurassic Nelson suite granitoids (Höy and Jackaman, 2005b; Little, 1957; Tempelman-Kluit,
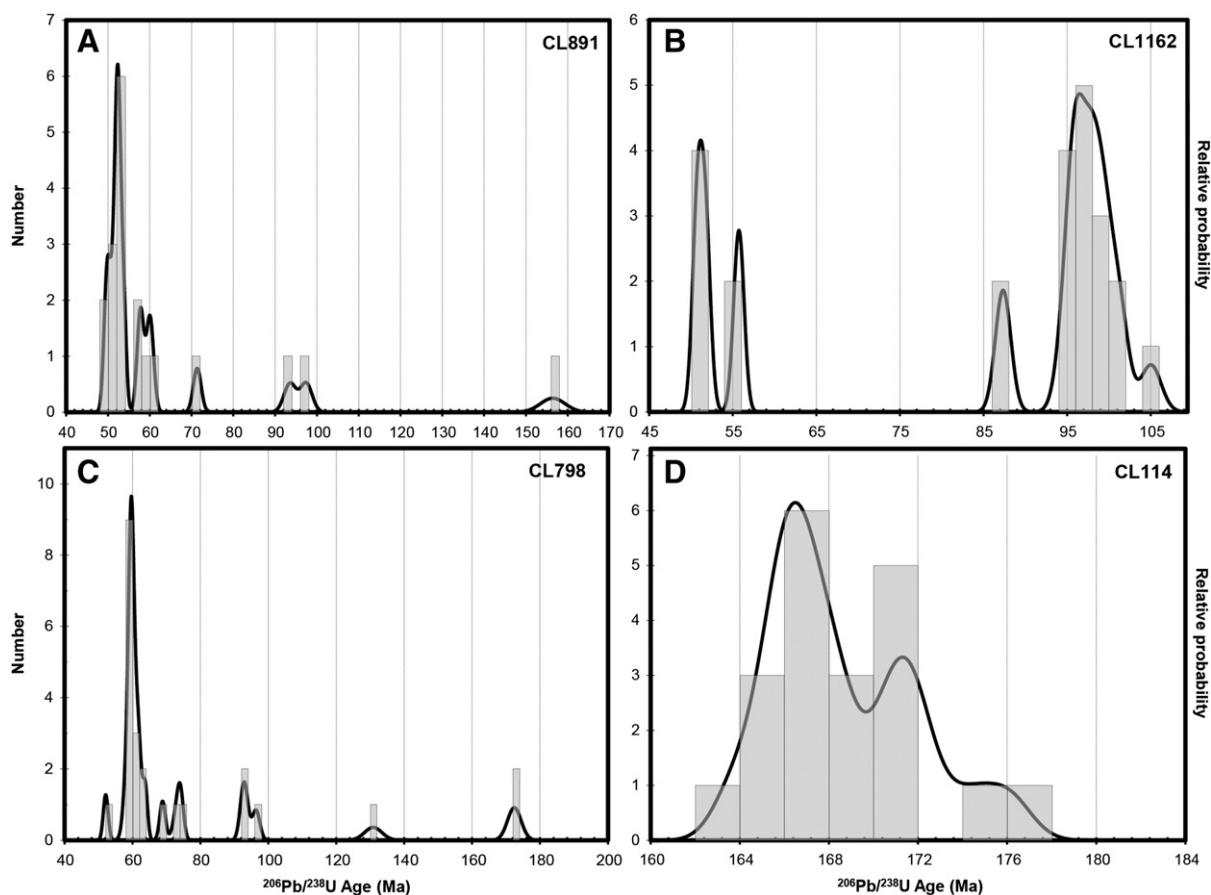
Fig. 18. Probability–density plots for U–Pb zircon SHRIMP ages. The three samples from the Grand Forks complex and bounding shear zone show considerable inheritance suggestive of magma recycling in the middle crust (S-type magmatism). Sample CL114, however, records only Middle Jurassic ages, suggesting an I-type origin. Input errors are 1σ.

1989) (Fig. 2). These studies correlated the Jura-Cretaceous hanging wall intrusives with the undeformed leucogranites and quartz monzonites in the footwall of the KRF (e.g. sample CL891), and the composite Okanagan Batholith. In contrast, Acton et al. (2002) correlated these intrusives with the Paleocene - Eocene Ladybird suite (e.g. Carr, 1992; Carr and Simony, 2006; Hinchey and Carr, 2006).

In the Texas Point shear zone (TPSZ) that bounds the northeastern margin of Christina Lake (Fig. 2), the degree of deformation in observed leucogranitic intrusives is highly variable (Cubley and Pattison, in press). In areas characterized by highly deformed granitoids of the Nelson suite, the leucogranites are observed as coevally deformed sheets parallel to the shallowly east-dipping foliation (Fig. 4d), with top-to-the-east shear sense indicators. However, leucogranites are observed elsewhere as massive bodies, suggesting that granitoid emplacement outlasted ductile deformation. Outside of the TPSZ and the associated Gladstone shear zone (GSZ) (Fig. 2), the leucogranite is massive and undeformed. The TPSZ is abruptly truncated by ~51 Ma Coryell suite intrusives near Texas Point (Figs. 2, 4f). Brittle deformation fabrics associated with the Kettle River fault crosscut ductile fabrics in leucogranite bodies at a high angle (Fig. 4h), and brittle deformation post-dates Coryell emplacement (Acton, 1998; Cubley and Pattison, in press).

Leucogranite sample CL798 was collected from the TPSZ ~1 km north of Texas Point (Fig. 2). This strongly foliated biotite leucogranite is emplaced into Nelson-suite hornblende orthogneiss (Fig. 15e,f), and both dip moderately to the northeast. Analyzed zircons are typically prismatic and range in size from 55×150 μm to 130×570 μm. Cores range from highly resorbed and irregular to euhedral. Grain rims are variably resorbed (Fig. 16c).

Twenty-four spot analyses were conducted on 17 individual grains in CL798 (Appendix D). The oldest inherited ages recorded in sample CL798

are Middle Jurassic, 172.4 ± 2.8 Ma (MSWD = 0.0008, n = 2), present in the euhedral cores of prismatic zircons. There are a number of poorly defined Late Cretaceous to Paleocene, 73.8 ± 1.2 Ma (MSWD = 0.53, n = 2), 68.9 ± 0.8 Ma (n = 1), and 62.4 ± 0.8 Ma (MSWD = 2.2, n = 4) populations present in zircon rims, however it is difficult to assess whether these represent mixing between thin rim growth zones. The dominant zircon population in sample CL798, 59.5 ± 0.5 Ma (MSWD = 0.4, n = 10), occurs as thin rims and is interpreted to be the crystallization age of the leucogranite. The origin of a single, younger 52.1 ± 0.7 Ma age is uncertain.

4.4.2. Deformed hornblende granodiorite (CL114)

In the KRF hanging wall, a granitoid pluton correlated with the Nelson intrusive suite based on composition and cross-cutting relationships intrudes low-grade metasediments and associated igneous rocks of the Pennsylvanian–Permian Mollie Creek Assemblage, Triassic Josh Creek diorite, and Early Jurassic Rossland Group. In the Sutherland Creek drainage east of Christina Lake, the pluton has developed a contact aureole with migmatitic Crd + Kfs ± Grt metapelites grading into Crd ± And pelites further from the intrusive contact, indicating pressures of 2.5 ± 0.5 kbar (Cubley and Pattison, 2009, in press).

Sample CL114 is a foliated hornblende-biotite granodiorite from the Sutherland Creek drainage, ~275 m from the contact with Mollie Creek Assemblage metasediments. The steeply dipping foliation is cut by high angle, cm-scale shear bands oriented ~N–S (Fig. 15g,h). Zircon grains in sample CL114 range in size from 30×70 μm to 105×380 μm, and are characterized by strongly zoned, prismatic crystals mantled by a thin (5–15 μm) fringe of anhedral, irregular zircon growth that is variably developed (Fig. 16d). A small number

of grains are highly resorbed, with original zoning truncated by anhedral regrowth rims up to 35 μm thick. Twenty-two spot analyses from 19 zircon grains (Appendix D) record a single age of 167.9 ± 1.3 Ma (MSWD = 1.5). A Tera–Wasserburg concordia plot is shown in Fig. 17d, with a relative probability diagram in Fig. 18d.

4.5. Significance of hanging wall U–Pb ages

4.5.1. Deformed biotite leucogranite (CL798)

Based on its Paleocene age and mineralogy, this leucogranite sample on the eastern margin of the Grand Forks complex is correlated with the regionally extensive ~62–52 Ma Ladybird suite (Carr, 1992; Carr et al., 1987, Hinchey and Carr, 2006; Parrish et al., 1988; Teyssier et al., 2005). A U–Pb zircon age from Parrish (1992a) on a lithologically similar granitoid along the KRF fault trace ~30 km north of Christina Lake also yielded a Paleocene age of 56 ± 1 Ma. These leucogranites cannot be the hanging wall equivalents to the ~50 Ma undeformed granitoids found in the GFC (e.g. CL891), in contrast to the mapping by Little (1957), Tempelman-Kluit (1989), and Höy and Jackaman (2005b).

In the Monashee complex, the Ladybird suite has been geochemically and isotopically linked to anatectic melt formation in the underlying basement gneisses (Carr, 1992; Hinchey and Carr, 2006; Vanderhaeghe et al., 1999), whereas in the Valhalla complex, Spear and Parrish (1996) proposed that Ladybird leucogranite generation is the result of prograde dehydration melting of muscovite in pelitic gneisses. The level of emplacement of the Ladybird leucogranite suite has been proposed to localize the formation of extensional detachment faults in a number of Shuswap core complexes (e.g. Simony and Carr, 1997; Vanderhaeghe et al., 1999). In the Valhalla complex, Simony and Carr (1997) and Carr and Simony (2006) argued that the "transient thermal pulses" and associated pegmatitic fluids linked to the injection of sheets of Ladybird leucogranite at the base of the Jurassic Nelson granitoid suite enhanced ductility at that horizon and localized formation of the 59–55 Ma Valkyr shear zone.

In this study, similar features are interpreted on the eastern margin of the Grand Forks complex along Christina Lake (Fig. 2). At ~60 Ma, the granites and granodiorites of the Middle Jurassic Nelson suite (167.9 ± 1.3 Ma, sample CL114, this study) were relatively cool and rigid compared to the deeper, migmatitic gneisses of the underlying Grand Forks complex. We interpret that the anatectic melts generated in the GFC during prograde metamorphism rose until they reached this rheologic boundary and pooled at that structural level. The abundance of Ladybird suite leucogranites is greatest within the Texas Point shear zone and then decreases southward and upward through the hanging wall stratigraphic sequence. The rheologic contrast between the Ladybird leucogranite and Nelson suite may have led to the initiation of a low-angle detachment (TPSZ) just below that horizon.

Due to the truncation of these shear zones by the Coryell Batholith (Figs. 2, 4f), which in turn is brittlely deformed by the KRF, these shear zones cannot be attributed to KRF deformation and their timing is constrained to between ~59 and 51 Ma. This is consistent with the observation of Rhodes and Cheney (1981) that KRF ductile fabrics are not exposed in the hanging wall. We suggest that the TPSZ represents an earlier, high-temperature shear zone, perhaps a "proto-KRF," that localized later lower-temperature extension on the KRF. An analogy for this would be in the Valhalla complex, where the amphibolite facies Valkyr shear zone (59–55 Ma) predated and localized subsequent greenschist facies extension on the Slocan Lake fault (54–45 Ma) (Carr and Simony, 2006; Carr et al., 1987; Spear, 2004).

4.5.2. Deformed hornblende granodiorite (CL114)

In the Grand Forks complex itself, there is no evidence for Middle Jurassic magmatism and/or metamorphism, with the exception of a preliminary date on a tabular gneissic hornblende syenite body within

Unit VIII of Preto (1970) that yielded an unpublished Middle Jurassic U–Pb age (Hunt and Roddick, 1990). The presence of abundant Middle Jurassic Nelson-suite intrusives in the hanging walls of both the Granby and Kettle River faults (Acton et al., 2002; Fyles, 1990; Höy and Jackaman, 2005b; Little, 1957; Tempelman-Kluit, 1989) suggests that the Quesnel cover rocks were transported eastward over the currently exposed North American margin rocks (GFC) after the Middle Jurassic. The new zircon date from CL114 (167.9 ± 1.3 Ma) places a lower age constraint on the timing of contact metamorphism observed in metapelites of the Mollie Creek Assemblage (Cubley and Pattison, in press). The 168 Ma age of CL114 falls within the documented range of ages for Middle Jurassic Nelson-suite granitoid plutons in the Kootenay Arc and Omineca belt of ~173–159 Ma (Archibald et al., 1983; Ghosh, 1995; Parrish, 1992b; Sevigny and Parrish, 1993).

4.6. Implications of U–Pb geochronology for P–T–t evolution of the Grand Forks complex.

The data from this investigation provide a record of protracted metamorphism within the Paleoproterozoic to early Paleozoic sediments of the GFC, involving several episodes of metamorphic monazite growth between the Late Jurassic and Eocene (Fig. 11). A similar metamorphic history is found in gneisses of the cover sequence of the Monashee complex (e.g. Crowley et al., 2000; Digel et al., 1998; Johnston et al., 2000; Scammell, 1993; Sevigny et al., 1990, 1989). The geochronological record from deeper stratigraphic levels of the Monashee complex (e.g. Thor-Odin and Frenchman Cap domes) and from other core complexes (Okanogan dome, Valhalla complex) is dominated by latest Cretaceous to Eocene ages (e.g. Crowley and Parrish, 1999; Gordon et al., 2008; Hinchey et al., 2007; Kruckenberg et al., 2008), with no record preserved of possible earlier episodes of metamorphism.

Table 2 summarizes the main igneous, metamorphic, and deformational events in the GFC during the Paleocene to Early Eocene. The Grand Forks complex is proposed to have undergone peak metamorphism and associated anatexis sometime in the interval between 59 and 50 Ma. Monazite is predicted to be unstable at peak metamorphic conditions for all samples in this study, and thus peak metamorphism cannot be dated directly.

Prograde melting reactions in core complex migmatites such as the GFC are proposed to have generated partial melt that was emplaced at higher structural levels as the 62–52 Ma Ladybird leucogranite suite (Carr, 1992; Hinchey and Carr, 2006; Spear and Parrish, 1996; Vanderhaeghe et al., 1999). Based on monazite dating within the GFC, dated Ladybird leucogranite in the hanging wall of the KRF (59.5 ± 0.5 Ma) cannot have been directly sourced from the exposed GFC migmatites, as peak metamorphism postdated ~59 Ma. However, it may have originated from a comparable source area at deeper, unexposed structural levels. High-T decompression accompanied by low-pressure, high-temperature corona development is interpreted to have occurred at ~52–50 Ma, as documented by Generation 7 monazite growth. Textural evidence for the timing of this decompression is provided by 49.9 ± 1.0 Ma Generation 7 monazite ages in inclusions in coronal textures, suggesting the development of these assemblages (and thus decompression itself) is an Early Eocene event. Syn-kinematic pegmatites suggest ductile deformation was still ongoing at 51.2 ± 0.6 Ma, with subsequent high-T folding events constrained to a narrow window between 51 and 50 Ma. Ductile fabrics are truncated by undeformed 50.0 ± 0.9 granitoids, indicating cessation of high-T deformation by that time.

Simony and Carr (2011) suggested the ductile fabrics exposed in the GFC may represent the westward extension of the compressional Gwillim Creek shear zone (GCSZ) exposed in the Valhalla complex (~85 Ma with reactivation at 65–60 Ma). The data from this study suggest the ductile shear zones in the GFC, which are relatively minor features, are younger, implying either that 1) possible early

GSCZ fabrics were overprinted by younger Eocene mylonitization, or 2) the Gwillim Creek shear zone projects below the exposed structural level.

Fig. 19 shows temperature–time (T–t) and pressure–temperature (P–T) paths that summarize the high-temperature metamorphism and exhumation of the Grand Forks complex, incorporating all the U–Pb geochronological data presented above. In both diagrams, the timing and P–T conditions of low-temperature (~415 °C) exhumation on the KRF are estimated from $^{40}Ar/^{39}Ar$ age estimates and oxygen isotope exchange thermometry for syn-kinematic muscovite in greenschist facies footwall mylonites in Washington (Berger and Snee, 1992; Mulch

et al., 2007). From the Late Jurassic to Paleocene, the Grand Forks complex experienced episodic metamorphism and monazite growth, culminating in peak metamorphism at ~750–800 °C, 5.5–6 kbar (Cubley and Pattison, 2009; Laberge and Pattison, 2007) between 59 and 50 Ma. This metamorphism was bracketed by subsolidus Generation 6 prograde monazite growth (~59 Ma) and suprasolidus Generation 7 retrograde monazite growth (~50 Ma) at ~735–650 °C. When combined with the $^{40}Ar/^{39}Ar$ muscovite and oxygen isotope thermometry data, the implication is that the GFC cooled extremely rapidly following near-isothermal, high-temperature decompression, with cooling rates in excess of 100 °C/Ma between 49.9 ± 1.0 Ma (735 °C, Mnz) and

Table 2
Summary table of the metamorphic, igneous, and deformational events occurring in the GFC in the Paleocene to Early Eocene.

|	Igneus events		Metamorphic events	Deformation events	
	GFC	KRF Hanging Wall	GFC	GFC	KRF Hanging Wall
65 Ma					
60 Ma		Ladybird leucogranite (CL798)	Generation 6 monazite growth during subsolidus prograde metamorphism		Window for high-T deformation on the TPSZ and GSZ
55 Ma			Window for timing of peak metamorphism	WIndow for development of S2 gneissosity	
50 Ma	Deformed pegmatite (CL1162) / Post-kinematic granitoids (CL891)	Coryell Batholith (Carr and Parkinson, 1989)	1) Generation 7 monazite growth 2) Corona formation 3) Leucosome crytallization 4) Melanosome formation	High-T 2.5 kbar decompression with mylonite formation; followede by F3a/F3b folding	
				Greenschist facies brittle deformation on the kettle River and Grandy faiults	
45 Ma					
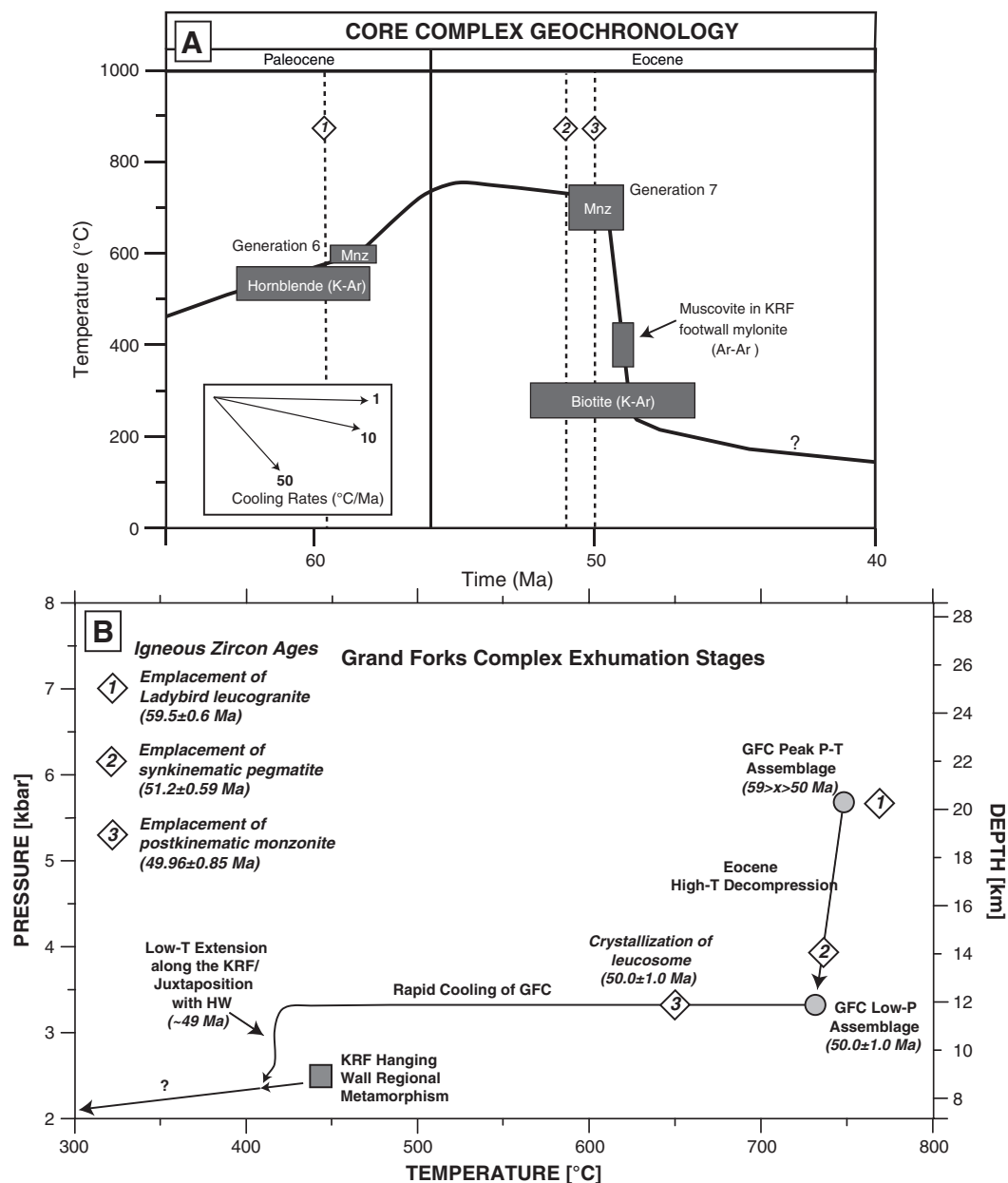
Fig. 19. A) Time–temperature (T–t) path for the exhumation of the Grand Forks complex, using U–Pb zircon and monazite data (this study) with $^{40}Ar/^{40}K$ hornblende and biotite and $^{40}Ar/^{39}Ar$ muscovite data from previous authors (see text for details). Monazite error boxes represent the combined temperature estimate errors (Cubley and Pattison, in press) and the geochronology 2σ error estimates of this study. B) P–T path for exhumation of the GFC, based off P–T estimates from Cubley and Pattison (in press), monazite data from this study, and $^{40}Ar/^{39}Ar$ muscovite data from KRF mylonites (Mulch et al., 2007)). Igneous ages from this study are shown. See text for details.

49.2 ± 0.2 Ma (415 °C, Ms). At the end of rapid cooling, extensional faulting under greenschist facies conditions occurred along the Kettle River and Granby faults to juxtapose the GFC against exposed hanging wall lithologies. This interpretation supports the interpretation of Mulch et al. (2007) that Eocene mid-crustal exhumation in the Omineca belt predated low-T extension on overlying extensional detachments (e.g. the KRF) by only a few million years.

Rapid (>100 °C/Ma) cooling following high-T, amphibolite facies decompression has been documented elsewhere in the Shuswap domain, namely the Okanogan dome (Kruckenberg et al., 2008), Valhalla complex (Gordon et al., 2009; Spear, 2004; Spear and Parrish, 1996) and the Monashee complex (Hinchey et al., 2007; Norlander et al., 2002; Vanderhaeghe et al., 2003). Rapid cooling following near-isothermal decompression was also predicted in thermomechanical modeling by Rey et al. (2009). The more gradual cooling of the GFC proposed by

Laberge and Pattison (2007) was based on $^{40}Ar/^{40}K$ hornblende ages which suggested passage through hornblende closure (~530 ± 30 °C) at ~60 Ma (Hunt and Roddick, 1990; Stevens et al., 1982), a finding that is incompatible with the more recent U–Pb results of this study. New $^{40}Ar/^{39}Ar$ hornblende and biotite data will be presented in a forthcoming publication (Cubley et al., in press) to better refine this history.

Supplementary data to this article can be found online at http://dx.doi.org/10.1016/j.lithos.2012.10.015.

Acknowledgments

with LA-ICP-MS analyses, and D. Moynihan for early reviews of this manuscript. Frank Spear and an anonymous reviewer are thanked for their critical reviews.

References

Acton, S. L., 1998. Geology of the Christina Lake area, B.C. M.Sc. thesis, Department of Geology and Geophysics, University of Calgary, Calgary, Alberta, Canada, 110p.

Acton, S.L., Simony, P.S., Heaman, L.M., 2002. Nature of the basement to Quesnel Terrane near Christina Lake, southeastern British Columbia. Canadian Journal of Earth Sciences 39, 65–78. http://dx.doi.org/10.1139/E01-056.

Adams, M.G., Lentz, D.R., Shaw, C.S.J., Williams, P.F., Archibald, D.A., Cousens, B., 2005. Eocene shoshonitic mafic dykes intruding the Monashee Complex, British Columbia: a petrogenetic relationship with the Kamloops Group volcanic sequence? Canadian Journal of Earth Sciences 42 (1), 11–24. http://dx.doi.org/10.1139/E04-091.

Archibald, D.A., Glover, J.K., Price, R.A., Farrar, E., Carmichael, D.M., 1983. Geochronology and tectonic implications of magmatism and metamorphism, southern Kootenay Arc and neighbouring regions, southeastern British Columbia. Part I: Jurassic to mid-Cretaceous. Canadian Journal of Earth Sciences 20, 1891–1913.

Armstrong, R.L., Parrish, R.R., van der Heyden, P., Scott, K., Runkle, D., Brown, R.L., 1991. Early Proterozoic basement exposures in the southern Canadian Cordillera: core gneiss of Frenchman Cap, Unit I of the Grand Forks Gneiss, and the Vaseaux Formation. Canadian Journal of Earth Sciences 28, 1169–1201.

Berger, B.R., Snee, L.W., 1992. Thermochronologic constraints on mylonite and detachment fault development, Kettle Highlands, northeastern Washington and southern British Columbia. Geological Society of America Abstracts with Programs 24, 7.

Black, L.P., Kamo, S.L., Allen, C.M., Aleinikoff, J.N., Davis, D.W., Korsch, R.J., Foudoulis, C., 2003. TEMORA 1: a new zircon standard for Phanerozoic U–Pb geochronology. Chemical Geology 200 (1–2), 155–170. http://dx.doi.org/10.1016/S0009-2541(03)00165-7.

Braun, I., Montel, J.M., Nicollet, C., 1998. Electron microprobe dating of monazites from high-grade gneisses and pegmatites of the Kerala Khondalite Belt, southern India. Chemical Geology 146 (1–2), 65–85 (pii: S0009-2541_ 98.00005-9).

Brown, S.R., 2010. Geology and geochronology of the southern Okanagan Valley shear zone, southern Canadian Cordillera, British Columbia. Ph.D. thesis, Department of Earth Sciences, Simon Fraser University, Burnaby, British Columbia, Canada, 310p.

Brown, R.L., Journeay, J.M., 1987. Tectonic denudation of the Shuswap metamorphic terrane of southeastern British Columbia. Geology 15 (2), 142–146.

Carr, S.D., 1992. Tectonic setting and U–Pb geochronology of the early Tertiary Ladybird leucogranite suite, Thor-Odin – Pinnacles area, southern Ominea Belt, British Columbia. Tectonics 11 (2), 258–278.

Carr, S.D., Parkinson, D.L., 1989. Eocene stratigraphy, age of the Coryell Batholith, and extensional faults in the Granby Valley, southern British Columbia. Geological Survey of Canada Paper 89–1, 79–87.

Carr, S.D., Simony, P.S., 2006. Ductile thrusting versus channel flow in the southeastern Canadian Cordillera: evolution of a coherent crystalline thrust sheet. Geological Society, London, Special Publications 268 (1), 561–587. http://dx.doi.org/10.1144/GSL.SP.2006.268.01.26.

Carr, S.D., Parrish, R.R., Brown, R.L., 1987. Eocene structural development of the Valhalla complex, southeastern British Columbia. Tectonics 6, 175–196.

Cheney, E.S., 1980. Kettle dome and related structures of northeastern Washington. Geological Society of America Memoir 153, 463–483.

Crowley, J.L., 1997. U–Pb geochronologic constraints on the cover sequence of the Monashee complex, Canadian Cordillera: Paleoproterozoic deposition on basement. Canadian Journal of Earth Sciences 34, 1008–1022.

Crowley, J.L., Parrish, R.R., 1999. U–Pb isotopic constraints on diachronous metamorphism in the northern Monashee complex, southern Canadian Cordillera. Journal of Metamorphic Geology 17 (5), 483–502. (http://doi.wiley.com/10.1046/j.1525-1314.1999.00210.x).

Crowley, J.L., Ghent, E.D., Carr, S.D., Simony, P.S., Hamilton, M.A., 2000. Multiple thermotectonic events in a continuous metamorphic sequence, Mica Creek area, southeastern Canadian Cordillera. Geological Materials Research 2 (2), 1–45.

Cubley, J.F., 2012. Metamorphism and geochronology of the Grand Forks complex, British Columbia. Ph.D. thesis, Department of Geoscience, University of Calgary, Calgary, Alberta, 400p.

Cubley, J.F., Pattison, D.R.M., 2009. Metamorphic contrast across the Kettle River fault, southeastern British Columbia, with implications for magnitude of fault displacement. Geological Survey of Canada Current Research 2009–9, 1–22.

Cubley, J.F., Pattison, D.R.M. Metamorphism and deformation of the Grand Forks complex: implications for the exhumation history of the Shuswap core complex, southern British Columbia. Canadian Journal of Earth Sciences (*in press*).

Cubley, J.F., Pattison, D.R.M., Archibald, D.A., Jolivet, M. Thermochronological constraints on the Eocene exhumation of the Grand Forks complex, British Columbia, based on [40]Ar/[39]Ar and apatite fission track geochronology. Canadian Journal of Earth Sciences (*in press*).

Currie, L.D., 1988. Geology of the Allen Creek area, Cariboo Mountains, British Columbia, M.Sc. thesis. Department of Geology and Geophysics, University of Calgary, Calgary, Alberta, Canada.

de Capitani, C.D., Brown, T.H., 1987. The computation of chemical equilibrium in complex systems containing non-ideal solutions. Geochimica et Cosmochimica Acta 51, 2639–2652.

de Capitani, C., Petrakakis, K., 2010. The computation of equilibrium assemblage diagrams with Theriak/Domino software. American Mineralogist 95 (7), 1006–1016. http://dx.doi.org/10.2138/am.2010.3354.

Dickin, A.P., 2005. Radiogenic isotope geology. Cambridge University Press, Cambridge, UK . (492 pp.).

Digel, S.G., Ghent, E.D., Carr, S.D., Simony, P.S., 1998. Early Cretaceous kyanite-sillimanite metamorphism and Paleocene sillimanite overprint near Mount Cheadle, southeastern British Columbia: geometry, geochronology, and metamorphic implications. Canadian Journal of Earth Sciences 35 (9), 1070–1087.

English, J.M., Johnston, S.T., 2004. The Laramide Orogeny: what were the driving forces? International Geology Review 46, 833–838.

Evenchick, C.A., McMechan, M.E., McNicoll, V.J., Carr, S.D., 2007. A synthesis of Jurassic-Cretaceous tectonic evolution of the central and southeastern Canadian Cordillera: exploring links across the orogen. In: Sears, J.W., Harms, T.A., Evenchick, C.A. (Eds.), Whence the Mountains? Inquiries into the Evolution of Orogenic Systems: A Volume in Honor of Raymond A. Price: Geological Society of America Special Paper, 433, pp. 117–145. http://dx.doi.org/10.1130/2007.2433(06).

Foster, G., Kinny, P., Vance, D., Prince, C., Harris, N., 2000. The significance of monazite U–Th–Pb age data in metamorphic assemblages; a combined study of monazite and garnet chronometry. Earth and Planetary Science Letters 181 (3), 327–340 (pii: S0012-821X(00)00212-0).

Foster, G., Gibson, H.D., Parrish, R.R., Horstwood, M., Fraser, J., Tindle, A., 2002. Textural, chemical and isotopic insights into the nature and behaviour of metamorphic monazite. Chemical Geology 191 (1–3), 183–207 (pii: S0009-2541(02)00156-0).

Fyles, J.T., 1990. Geology of the Greenwood-Grand Forks area, British Columbia. British Columbia Ministry of Energy, Mines, and Petroleum Resources Open File Report 1990–25, pp. 1–19.

Fyles, J.T., Harakal, J.E., White, W.H., 1973. The age of sulfide mineralization at Rossland, British Columbia. Economic Geology 68 (1), 23–33.

Ghosh, D.K., 1995. U–Pb geochronology of Jurassic to early Tertiary granitic intrusives from the Nelson–Castlegar area, southeastern British Columbia, Canada. Canadian Journal of Earth Sciences 32, 1668–1680.

Gibson, H.D., Brown, R.L., Parrish, R.R., 1999. Deformation-induced inverted metamorphic field gradients: an example from the southeastern Canadian Cordillera. Journal of Structural Geology 21 (7), 751–767 (pii: S0191-8141(99)00051-6).

Gibson, H.D., Carr, S.D., Brown, R.L., Hamilton, M.A., 2004. Correlations between chemical and age domains in monazite, and metamorphic reactions involving major pelitic phases: an integration of ID-TIMS and SHRIMP geochronology with Y-Th-U X-ray mapping. Chemical Geology 211 (3–4), 237–260. http://dx.doi.org/10.1016/j.chemgeo.2004.06.028.

Glombick, P., 2005. Mesozoic to early Tertiary tectonic evolution of the Shuswap metamorphic complex in the Vernon area, southeastern Canadian Cordillera. Ph.D. thesis, Department of Earth and Atmospheric Sciences, University of Alberta, Edmonton, Alberta. 440p.

Glombick, P., Thompson, R.I., Erdmer, P., Heaman, L., Friedman, R.M., Villeneuve, M., Daughtry, K.L., 2006. U–Pb constraints on the thermotectonic evolution of the Vernon antiform and the age of the Aberdeen gneiss complex, southeastern Canadian Cordillera. Canadian Journal of Earth Sciences 43 (2), 213–244. http://dx.doi.org/10.1139/E05-096.

Gordon, S.M., Whitney, D.L., Teyssier, C., Grove, M., Dunlap, W.J., 2008. Timescales of migmatization, melt crystallization, and cooling in a Cordilleran gneiss dome: Valhalla complex, southeastern British Columbia. Tectonics 27, 1–28. http://dx.doi.org/10.1029/2007TC002103.

Gordon, S.M., Grove, M., Whitney, D.L., Schmitt, A.K., Teyssier, C., 2009. Time–temperature–fluid evolution of migmatite dome crystallization: coupled U–Pb age, Ti thermometry, and O isotopic ion microprobe depth profiling of zircon and monazite. Chemical Geology 262 (3–4), 186–201. http://dx.doi.org/10.1016/j.chemgeo.2009.01.018.

Hallett, B.W., Spear, F.S., 2011. Insight into the cooling history of the Valhalla complex, British Columbia. Lithos 125, 809–824.

Hermann, J., Rubatto, D., 2003. Relating zircon and monazite domains to garnet growth zones: age and duration of granulite facies metamorphism in the Val Malenco lower crust. Journal of Metamorphic Geology 21, 833–852. http://dx.doi.org/10.1046/j.1525-1314.2003.00484.x.

Hinchey, A.M., Carr, S.D., 2006. The S-type Ladybird leucogranite suite of southeastern British Columbia: geochemical and isotopic evidence for a genetic link with migmatite formation in the North American basement gneisses of the Monashee complex. Lithos 90, 223–248. http://dx.doi.org/10.1016/j.lithos.2006.03.003.

Hinchey, A.M., Carr, S.D., McNeill, P.D., Rayner, N., 2006. Paleocene–Eocene high-grade metamorphism, anatexis, and deformation in the Thor-Odin dome, Monashee complex, southeastern British Columbia. Canadian Journal of Earth Sciences 43, 1341–1365. http://dx.doi.org/10.1016/j.lithos.2006.03.003.

Hinchey, A.M., Carr, S.D., Rayner, N., 2007. Bulk compositional controls on the preservation of age domains within metamorphic monazite: a case study from quartzite and garnet-cordierite-gedrite gneiss of Thor-Odin dome, Monashee complex, Canadian Cordillera. Chemical Geology 240, 85–102. http://dx.doi.org/10.1016/j.chemgeo.2007.02.001.

Holder, R.W., Holder, G.A.M., 1988. The Colville batholith: Tertiary plutonism in northeast Washington associated with graben and core-complex (gneiss dome) formation. Geological Society of America Bulletin 100, 1971–1980.

Höy, T., 2006. Geology of the Hope 1 Claim, Christina Lake Area, Southeastern British Columbia. Fieldwork report for Kootenay Gold Inc., Greenwood mining district (13 pp.).

Höy, T., Dunne, K.P.E., 1997. Early Jurassic Rossland Group, southern British Columbia. Part I–stratigraphy and tectonics. British Columbia Ministry of Employment and Investment, Mines and Energy Division. Geological Survey Branch Bulletin 102.

Höy, T., Jackaman, W., 2005a. Geology and mineral potential of the Grand Forks map sheet (082E/01), Southeastern British Columbia. British Columbia Geological Survey Geological Fieldwork 2005–1, 225–230.

Höy, T., Jackaman, W., 2005b. Geology of the Grand Forks map sheet (082E/01). British Columbia Ministry of Energy and Mines Geoscience Map 2005–2, scale 1:50,000.

Hunt, P.A., Roddick, J.C., 1990. A Compilation of K–Ar ages; Report 19 in Radiogenic Age and Isotopic Studies, Report 3. Geological Survey of Canada Paper 89–0, 225–230.

Janots, E., Engi, M., Berger, A., Allaz, J., Schwarz, J.O., Spandler, C., 2008. Prograde metamorphic sequence of REE minerals in pelitic rocks of the Central Alps: implications for allanite–monazite–xenotime phase relations from 250 to 610 °C. Journal of Metamorphic Geology 26 (5), 509–526. http://dx.doi.org/10.1111/j.1525-1314.2008.00774.x.

Johnson, B.J., Brown, R.L., 1996. Crustal structure and early Tertiary extensional tectonics of the Ominca belt at 51°N latitude, southern Canadian Cordillera. Canadian Journal of Earth Sciences 33, 1596–1611.

Johnston, S.T., 2001. The great Alaskan terrane wreck: reconciliation of paleomagnetic and geological data in the northern Cordillera. Earth and Planetary Science Letters 365, 163–183.

Johnston, D.H., Williams, P.F., Brown, R.L., Crowley, J.L., Carr, S.D., 2000. Northeastward extrusion and extensional exhumation of crystalline rocks of the Monashee complex, southeastern Canadian Cordillera. Journal of Structural Geology 22, 603–625 (pii: S0191-8141(99)00185-6).

Kelsey, D.E., Clark, C., Hand, M., 2008. Thermobarometric modelling of zircon and monazite growth in melt-bearing systems: examples using model metapelitic and metapsammitic granulites. Journal of Metamorphic Geology 26, 199–212. http://dx.doi.org/10.1111/j.1525-1314.2007.00757.x.

Kretz, R., 1983. Symbols for rock-forming minerals. American Mineralogist 68 (1–2), 277–279.

Kruckenberg, S.C., Whitney, D.L., 2011. Metamorphic evolution of sapphirine- and orthoamphibole-cordierite-bearing gneiss, Okanogan dome, Washington, USA. Journal of Metamorphic Geology 29 (4), 425–449.

Kruckenberg, S.C., Whitney, D.L., Teyssier, C., Fanning, C.M., Dunlap, W.J., 2008. Paleocene–Eocene migmatite crystallization, extension, and exhumation in the hinterland of the northern Cordillera: Okanogan dome, Washington, USA. Geological Society of America Bulletin 120 (7), 1–25. http://dx.doi.org/10.1111/j.1525-1314.2010.00926.x.

Laberge, J.D., 2005. Geology of the Granby Fault, southeastern British Columbia: metamorphism and tectonic evolution. M.Sc. thesis, Department of Geology and Geophysics, University of Calgary, Calgary, Alberta, Canada.

Laberge, J.D., Pattison, D.R.M., 2007. Geology of the western margin of the Grand Forks complex, southern British Columbia: high-grade Cretaceous metamorphism followed by early Tertiary extension on the Granby fault. Canadian Journal of Earth Sciences 44 (2), 199–228. http://dx.doi.org/10.1139/E06-101.

Little, H.W., 1957. Kettle River, east half, Similkameen, Kootenay and Osoyoos districts, British Columbia. Geological Survey of Canada Map 6–1957, scale 1:253,440.

Ludwig, K.R., 2001. SQUID 1.02, A User's Manual. Berkeley Geochronology Center Special Publication, Berkeley, CA, USA.

Ludwig, K.R., 2003. User's Manual for Isoplot/Ex, Version 3.0, A Geochronology Toolkit for Microsoft Excel. Berkeley Geochronology Center Special Publication, Berkeley, CA, USA.

Monger, J.W.H., Price, R.A., Tempelman-Kluit, D.J., 1982. Tectonic accretion and the origin of the two major metamorphic and plutonic welts in the Canadian Cordillera. Geology 10, 70–75.

Montel, J.M., 1993. A model for monazite/melt equilibrium and application to the generation of granitic magmas. Chemical Geology 110, 127–146.

Morris, G.A., Hooper, P.R., 1997. Petrogenesis of the Colville Igneous Complex, northeast Washington: Implications for Eocene tectonics in the northern U.S. Cordillera. Geology 25 (9), 831–834.

Morris, G.A., Larson, P.B., Hooper, P.R., 2000. Subduction style magmatism in a non-subduction setting: the Colville Igneous Complex, NE Washington State, USA. Journal of Petrology 41 (1), 43–67.

Mulch, A., Teyssier, C., Cosca, M.A., Chamberlain, C.P., 2007. Stable isotope paleoaltimetry of Eocene core complexes in the North American Cordillera. Tectonics 26 (4), 1–13. http://dx.doi.org/10.1029/2006TC001995.

Norlander, B.H., Whitney, D.L., Teyssier, C., Vanderhaeghe, O., 2002. Partial melting and decompression of the Thor-Odin dome, Shuswap metamorphic core complex, Canadian Cordillera. Lithos 61, 103–125 (pii: S0024-4937(02)00075-0).

Orr, K.E., Cheney, E.S., 1987. Kettle and Okanogan domes, northeastern Washington and southern British Columbia. Washington Division of Geology and Earth Resources Bulletin 77, 55–72.

Parrish, R.R., 1990. U–Pb dating of monazite and its application to geological problems. Canadian Journal of Earth Sciences 27, 1431–1450.

Parrish, R.R., 1992a. Miscellaneous U–Pb zircon dates from Southeast British Columbia in Radiogenic age and isotopic studies; Report 5. Geological Survey of Canada Paper 91–0, 143–153.

Parrish, R.R., 1992b. U–Pb ages of Jurassic–Eocene plutonic rocks in the vicinity of the Valhalla complex, southeast British Columbia in Radiogenic age and isotopic studies; Report 5. Geological Survey of Canada Paper 91–2, 115–134.

Parrish, R.R., 1995. Thermal evolution of the southeastern Canadian Cordillera. Canadian Journal of Earth Sciences 32, 1618–1642.

Parrish, R.R., Scammell, R.J., 1988. The age of the Mount Copeland syenite gneiss and its metamorphic zircons, Monashee Complex, southeastern British Columbia. Geological Survey of Canada Paper 88–2, 21–28.

Parrish, R.R., Carr, S.D., Parkinson, D.L., 1985. Metamorphic complexes and extensional tectonics, southern Shuswap complex, southeastern British Columbia. Field Guides to Geology and Mineral Deposits in the Southern Canadian Cordillera, Geological Society of America, Cordilleran Section, Vancouver, B.C, pp. 12.1–12.15.

Parrish, R.R., Carr, S.D., Parkinson, D.L., 1988. Eocene extensional tectonics and geochronology of the southern Ominca Belt, British Columbia and Washington. Tectonics 7 (2), 181–212.

Preto, V.A.G., 1970. Structure and petrology of the Grand Forks Group, British Columbia. Geological Survey of Canada Paper 69–2, 1–80.

Price, R.A., 1981. The Cordilleran foreland thrust and fold belt in the southern Canadian Rocky Mountains. In: McClay, K.R., Price, N.J. (Eds.), Thrust and Nappe Tectonics. Geological Society of London Special Publications, 9, pp. 427–448.

Pyle, J.M., Spear, F.S., 1999. Yttrium zoning in garnet: coupling of major accessory phases during metamorphic reactions. Geological Materials Research 1 (6), 1–49.

Pyle, J.M., Spear, F.S., 2000. An empirical garnet (YAG)-xenotime thermometer. Contributions to Mineralogy and Petrology 138, 51–58.

Pyle, J.M., Spear, F.S., 2003. Four generations of accessory-phase growth in low-pressure migmatites from SW New Hampshire. American Mineralogist 88, 338–351.

Pyle, J.M., Spear, F.S., Rudnick, R.L., McDonough, W.F., 2001. Monazite-xenotime-garnet equilibrium in metapelites and a new monazite-garnet thermometer. Journal of Petrology 42 (11), 2083–2107.

Rapp, R.P., Watson, E.B., 1986. Monazite solubility and dissolution kinetics — implications for the thorium and light rare-earth chemistry of felsic magmas. Contributions to Mineralogy and Petrology 94, 304–316.

Reid, L.F., 2003. Stratigraphy, structure, petrology, geochronology and geochemistry of the Hobson Lake area (Cariboo Mountains, British Columbia) in relation to the tectonic evolution of the southern Canadian Cordillera. Ph.D. thesis, Department of Geology and Geophysics, University of Calgary, Calgary, Alberta, Canada.

Rey, P.F., Teyssier, C., Whitney, D.L., 2009. Extension rates, crustal melting, and core complex dynamics. Geology 37 (5), 391–394. http://dx.doi.org/10.1130/G25460A.1.

Rhodes, B.P., Cheney, E.S., 1981. Low-angle faulting and origin of the Kettle dome, a metamorphic core complex in northeastern Washington. Geology 9 (8), 366–369.

Ross, M., Parrish, R.R., 1991. Detrital zircon geochronology of metasedimentary rocks in the southern Ominca Belt, Canadian Journal of Earth Sciences 28, 1254–1270.

Scammell, R.J., 1993. Mid-Cretaceous to Tertiary thermotectonic history of former mid-crustal rocks, southern Ominca Belt, Canadian Cordillera. Ph.D. thesis, Department of Geological Sciences, Queen's University, Kingston, Ontario, Canada.

Sevigny, J.H., Parrish, R.R., 1993. Age and origin of Late Jurassic and Paleocene granitoids, Nelson Batholith, southern British Columbia. Canadian Journal of Earth Sciences 30, 2305–2314.

Sevigny, J.H., Parrish, R.R., Ghent, E.D., 1989. Petrogenesis of peraluminous granites, Monashee Mountains, southeastern Canadian Cordillera. Journal of Petrology 30 (3), 557–581.

Sevigny, J.H., Parrish, R.R., Donelick, R.A., Ghent, E.D., 1990. Northern Monashee Mountains, Ominca Crystalline Belt, British Columbia: timing of metamorphism, anatexis, and tectonic denudation. Geology 18, 103–106.

Simonetti, A., Heaman, L.M., Hartlaub, R.P., Creaser, R.A., Machattie, T.G., Bohm, C., 2005. U–Pb zircon dating by laser ablation-MC-ICP-MS using a new multiple ion counting Faraday collector array. Journal of Analytical Atomic Spectrometry 20 (8), 677–686. http://dx.doi.org/10.1039/b504465k.

Simonetti, A., Heaman, L.M., Chacko, T., Banerjee, N.R., 2006. In situ petrographic thin section U–Pb dating of zircon, monazite, and titanite using laser ablation–MC–ICP-MS. International Journal of Mass Spectrometry 253 (1–2), 87–97. http://dx.doi.org/10.1016/j.ijms.2006.03.003.

Simony, P.S., Carr, S.D., 1997. Large lateral ramps in the Eocene Valkyr shear zone: extensional ductile faulting controlled by plutonism in southern British Columbia. Journal of Structural Geology 19 (6), 769–784 (pii: S0191-8141(97)00011-4).

Simony, P.S., Carr, S.D., 2011. Cretaceous to Eocene evolution of the Southeastern Canadian Cordillera: continuity of rocky mountain thrust systems with zones of 'in-sequence' mid-crustal flow. Journal of Structural Geology 33, 417–434. http://dx.doi.org/10.1016/j.jsg.2011.06.001.

Spear, F.S., 2004. Fast cooling and exhumation of the Valhalla metamorphic core complex, Southeastern British Columbia. International Geology Review 46 (3), 193–209.

Spear, F.S., 2010. Monazite–allanite phase relations in metapelites. Chemical Geology 279 (1–2), 55–62. http://dx.doi.org/10.1016/j.chemgeo.2010.10.004.

Spear, F.S., Parrish, R.R., 1996. Petrology and cooling rates of the Valhalla complex, British Columbia, Canada. Journal of Petrology 37 (4), 733–765.

Spear, F.S., Pyle, J.M., 2010. Theoretical modeling of monazite growth in a low-Ca metapelite. Chemical Geology 273 (1–2), 111–119. http://dx.doi.org/10.1016/j.chemgeo.2010.02.016.

Stevens, R.D., Delabio, R.N., Lachance, G.R., 1982. Age determinations and geological studies, K–Ar isotopic ages, Report 15. Geological Survey of Canada Paper 81–2 (56 pp.).

Stinson, P.K., 1995. Emplacement of the Coryell Batholith. M.Sc. thesis, Department of Geology and Geophysics, University of Calgary, Calgary, Alberta, Canada, 151p.

Suydam, J.D., Gaylord, D.R., 1997. Toroda Creek half graben, northeast Washington: Late-stage sedimentary infilling of a synextensional basin. Geological Society of America Bulletin 109 (10), 1333–1348.

Tempelman-Kluit, D.J., 1989. Geology, Penticton, British Columbia. Geological Survey of Canada Map 1736A, scale 1:250,000.

Tera, F., Wasserburg, G.J., 1972. U-Th-Pb systematics in three Apollo 14 basalts and the problem of initial Pb in lunar rocks. Earth and Planetary Science Letters 14, 281–304.

Teyssier, C., Ferré, E., Whitney, D.L., Norlander, B.H., Vanderhaeghe, O., Parkinson, D.L., 2005. Flow of partially molten crust and origin of detachments during collapse of the Cordilleran Orogen. In: Bruhn, D., Burlini, L. (Eds.), High-strain Zones: Structures and Physical Properties: Geological Society of London Special Publication, 245, pp. 39–64.

Tomkins, H.S., Pattison, D.R.M., 2007. Accessory phase petrogenesis in relation to major phase assemblages in pelites from the Nelson contact aureole, southern British Columbia. Journal of Metamorphic Geology 25 (4), 401–421. http://dx.doi.org/10.1111/j.1525-1314.2007.00702.x.

Unterschutz, J.L.E., Creaser, R.A., Thompson, R.I., Daughtry, K.L., 2002. North American margin origin of Quesnel terrane strata in the southern Canadian Cordillera: inferences from geochemical and Nd isotopic characteristics of Triassic meta-sedimentary rocks. Geological Society of America Bulletin 114 (4), 462–475.

Vanderhaeghe, O., Teyssier, C., 2001. Partial melting and flow of orogens. Tectonophysics 342, 451–472.

Vanderhaeghe, O., Teyssier, C., Wysoczanski, R., 1999. Structural and geochronological constraints on the role of partial melting during the formation of the Shuswap metamorphic core complex at the latitude of the Thor-Odin dome, British Columbia. Canadian Journal of Earth Sciences 36, 917–943.

Vanderhaeghe, O., Teyssier, C., McDougall, I., Dunlap, W.J., 2003. Cooling and exhumation of the Shuswap metamorphic core complex constrained by $^{40}Ar/^{39}Ar$ thermochronology. Geological Society of America Bulletin 115, 200–216. http://dx.doi.org/10.1130/0016-7606(2003) 115<0200:CAEOTS>2.0.CO;2.

Wheeler, J.O., McFeely, P., 1991. Tectonic assemblage map of the Canadian Cordillera and adjacent parts of the United States of America. Geological Survey of Canada Map 1712A, scale 1: 2,000,000.

Williams, I.S., 1998. U-Th-Pb Geochronology by ion microprobe. Reviews in Economic Geology 7, 1–35.

Williams, M.L., Jercinovic, M.J., Terry, M.P., 1999. Age mapping and dating of monazite on the electron microprobe: deconvoluting multistage tectonic histories. Geology 27 (11), 1023–1026.

Williams, M.L., Jercinovic, M.J., Hetherington, C.J., 2007. Microprobe monazite geochronlogy: understanding geologic processes by integrating composition and chronology. Annual Review of Earth and Planetary Sciences 35, 137–175. http://dx.doi.org/10.1146/annurev.earth.35.031306.140228.

Wing, B.A., Ferry, J.M., Harrison, T.M., 2003. Prograde destruction and formation of monazite and allanite during contact and regional metamorphism of pelites: petrology and geochronology. Contributions to Mineralogy and Petrology 145, 228–250. http://dx.doi.org/10.1007/s00410-003-0446-1.

Wooden, J.L., Box, S.E., 1996. Contrasting inherited zircon populations in an Eocene vs. an Early Cretaceous intrusive associated with the eastern Kettle metamorphic core complex, NE Washington. Geological Society of America Abstracts with Programs 26 (7), A-444.

Zhu, X.K., O'Nions, R.K., 1999. Monazite chemical composition: some implications for monazite geochronology. Contributions to Mineralogy and Petrology 137 (4), 351–363.